Thermonuclear Explosions of Chandrasekhar Mass White Dwarfs

46

Ken'ichi Nomoto and Shing-Chi Leung

Abstract

The thermonuclear explosion of a Chandrasekhar mass white dwarf is an important class of supernovae which can attribute to various subclasses of Type Ia supernovae and accretion induced collapse. Type Ia supernovae are not only essential as their roles of standard candle in the discovery of dark energy, but also robust sources of iron-peak elements for the galactic chemical evolution. In this chapter we discuss the physics of the explosion mechanisms of the Chandrasekhar mass white dwarf. First we review the possible evolutionary paths for the accreting white dwarf to increase its mass to the Chandrasekhar mass in the binary systems. When the white dwarf's mass reaches near the Chandrasekhar limit, carbon burning is ignited and grows into deflagration in the central region. We review the principle component of deflagration physics and how it is implemented in supernova simulations. We then review the physics of detonation by examining its structure. We also discuss how the detonation is triggered physically and computationally. At last, we describe how these components are applied to various explosion mechanisms, including the deflagration-detonation transition, pure deflagration, and gravitationally confined detonation. Their typical behaviour, nucleosynthesis, and applications to the galactic chemical evolution and observed supernovae are examined.

Contents

K. Nomoto • S.-C. Leung
Kavli Institute for the Physics and Mathematics of the Universe (WPI), The University of Tokyo, Kashiwa, Chiba, Japan
e-mail: nomoto@astron.s.u-tokyo.ac.jp; shingchi.leung@ipmu.jp

1   Introduction

The thermonuclear explosion of a white dwarf with a mass near the Chandrasekhar limit is an important class of supernovae which can attribute to various subclasses of Type Ia supernovae. Type Ia supernovae are not only essential as their roles of standard candle in the discovery of dark energy, but also robust sources of iron-peak elements for the galactic chemical evolution.

In this chapter we discuss the physics of the explosion mechanisms of the Chandrasekhar mass white dwarf. First we review the possible evolutionary paths for the accreting white dwarf to increase its mass to the Chandrasekhar mass in the binary systems. When the white dwarf's mass reaches near the Chandrasekhar limit, carbon burning is ignited and grows into deflagration in the central region.

We review the principle component of deflagration physics and how it is implemented in supernova simulations. We then review the physics of detonation by examining its structure. We also discuss how the detonation is triggered physically and computationally. At last, we describe how these components are applied to various explosion mechanisms, including the deflagration-detonation transition, pure deflagration, and gravitationally confined detonation. Their typical behaviour, nucleosynthesis, and applications to the galactic chemical evolution and observed supernovae are examined.

2   Single-Degenerate Scenario for Progenitors of Type Ia Supernovae

The thermonuclear explosion of a C+O white dwarf has successfully explained the basic observed features of Type Ia supernovae (SNe Ia). Both the Chandrasekhar and the sub-Chandrasekhar mass models have been examined (Livio 2000). However,

no clear observational indication rejects how the white dwarf mass grows until C ignition, i.e., whether the white dwarf accretes H/He-rich matter from its binary companion [single-degenerate (SD) scenario] or whether two C+O white dwarfs merge [double-degenerate (DD) scenario] (e.g., Arnett 1996; Hillebrandt and Niemeyer 2000; Iben and Tutukov 1984; Ilkov and Soker 2012; Maoz et al. 2014; Nomoto 1982; Nomoto et al. 1994, 1997, 2000a, 2009; Webbink 1984).

2.1   Accretion-Induced Hydrogen Shell Burning

Here we focus on the SD scenario for the Chandrasekhar mass (Chandra) models of SN Ia, where an accreting C+O white dwarf (WD) increases its mass to the Chandrasekhar mass limit. If the mass donor is a normal star, a hydrogen shell burning is ignited when the mass of the accumulated hydrogen-rich matter reaches the ignition mass $M_{ig} (= \Delta M_H)$, which is presented as contours on the $M_{WD} - \dot{M} (= dM_H/dt)$ plane in Fig. 1. For a given $\dot{M}$, M_{ig} is smaller for a larger M_{WD} because of the smaller radius R and thus higher pressure for the same mass of accreted matter (see Eq. (3) below). For a given M_{WD}, M_{ig} is smaller for a higher $\dot{M}$ because of the faster compressional heating and thus higher temperature of accreted matter.

The stability of the hydrogen burning shell in the accreting white dwarf is crucial for its evolution. Figure 1 summarizes the properties of hydrogen shell burning (Kato et al. 2014; Nomoto 1982; Nomoto et al. 2007).

1. The hydrogen shell burning is unstable to flash in the area below the solid line to show $\dot{M}_{stable}$. This stability line (dashed line) is approximately represented by Kato et al. (2014)

$$\dot{M}_{stable} = 4.17 \times 10^{-7} \left(\frac{M_{WD}}{M_\odot} - 0.53 \right) M_\odot \ yr^{-1}. \tag{1}$$

2. Above the dash-dotted line for $\dot{M}_{cr}$ (= $(dM/dt)_{RH}$), the accreted matter is accumulated faster than consumed into He by H-shell burning. This critical accretion rate is represented as Kato et al. (2014)

$$\dot{M}_{cr} = 8.18 \times 10^{-7} \left(\frac{M_{WD}}{M_\odot} - 0.48 \right) M_\odot \ yr^{-1}. \tag{2}$$

3. For the region with $\dot{M} > \dot{M}_{cr}$, the accreted matter is piled up to form a red-giant-size envelope (Nomoto et al. 1979). This could lead to the formation of a common envelope and prevent further mass accretion onto the white dwarf. This problem for has been resolved by the strong optically thick winds (Hachisu et al. 1996, 1999a,b). If the wind is sufficiently strong, the white dwarf radius stays small enough to avoid the formation of a common envelope. Then steady
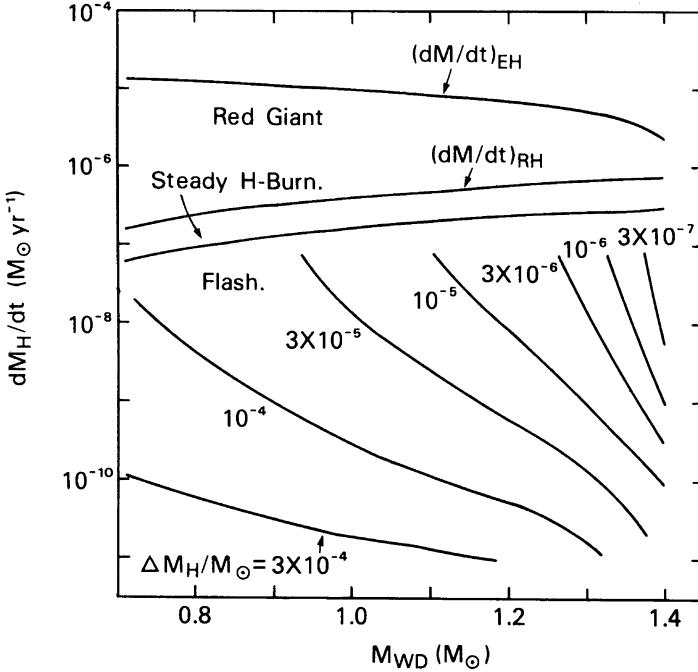
Fig. 1 The properties of accreted hydrogen-rich materials as functions of M_{WD} and dM_H/dt (Nomoto 1982). Hydrogen burning is stable in the region indicated by "Steady H-Burn" between the two lines of $\dot{M}_{stable}$ in Eq. (1) and $\dot{M}_{cr} (= (dM/dt)_{RH})$ in Eq. (2) (Kato et al. 2014). In the region below $\dot{M}_{stable}$, hydrogen shell burning is thermally unstable, and the WD experiences shell flashes. *Black solid lines* indicate the hydrogen-ignition masses ΔM_H, the values of which are shown beside each line. In the region above $(dM/dt)_{RH}$ (and below the Eddington limit $(dM/dt)_{EH}$), optically thick winds are accelerated, which prevents the formation of a red-giant-size envelope with the piled-up accreted material

hydrogen burning increases its mass at a rate $\dot{M}_{cr}$ by blowing the extra mass away in a wind.

4. In the area $\dot{M}_{stable} < \dot{M} < \dot{M}_{cr}$, accreting white dwarfs are thermally stable so that hydrogen burns steadily in the burning shell. Then the white dwarf mass increases at a rate of $\dot{M}$.

5. For $\dot{M} < \dot{M}_{stable}$, the flash of hydrogen shell burning is stronger (weaker) for lower (higher) $\dot{M}$ and thus for larger (smaller) M_{ig} and larger (smaller) M_{WD}. This is because the pressure P at the bottom of the thin accreted envelope is higher (lower) as given by

$$P = \frac{GM_{WD}M_{ig}}{4\pi R^4}, \tag{3}$$

(where the WD radius R is smaller for larger M_{WD}), so that the flash reaches higher (lower) temperature.

If the shell flash is strong enough to trigger a nova outburst, most part of the envelope is lost from the system. Moreover, a part of the original white dwarf matter is dredged up and lost in the outburst wind. Then M_{WD} decreases after the nova outburst. This would be the case for $\dot{M} < 10^{-9} M_{\odot} \, \text{yr}^{-1}$.

If the shell flash is weak enough, on the other hand, the ejected mass is smaller than the mass which hydrogen burning converts into helium. Then M_{WD} increases. This would be the case for smaller M_{ig} and thus $\dot{M} > 10^{-8} M_{\odot} \, \text{yr}^{-1}$.

In either case, the hydrogen flash recurs, and the recurrence period is proportional to $M_{ig}/\dot{M}$, which is shorter for higher $\dot{M}$. If the recurrence period is short, the flashes are observed as recurrent novae, which occurs in the upper-right region of this region.

2.2   He Shell Burning

For $\dot{M} > 10^{-8} M_{\odot} \, \text{yr}^{-1}$. H burning produces a thin He layer, and He flashes are ignited when the He mass reaches a certain critical value. In the early stages of the He shell flash, the envelope is electron degenerate and geometrically almost flat. Thus the temperature at the bottom of the He burning shell increases because of the almost constant pressure there as given by Eq. (3).

Heated by nuclear burning, the helium envelope gradually expands, which decreases the pressure. Then, the temperature attains its maximum and starts decreasing. The maximum temperature is higher for more massive WD and more massive envelope because of higher pressure. The strength depends on the He envelope mass M_{env}, thus depending on the accretion rate.

The He envelope mass M_{env} is larger for the slower mass-accumulation rate of the He layer $\dot{M}_{He}$. For $\dot{M}_{He} \sim 1 \times 10^{-8} \, M_{\odot} \, \text{yr}^{-1}$, M_{env} exceeds a critical value where the density at its bottom becomes high enough to induce a He detonation. This would result in the sub-Chandrasekhar mass explosion.

For higher $\dot{M}_{He}$, the He shell flashes are not strong enough to induce a He detonation. Then, such flashes recur many times with the increasing WD mass M_{WD} toward the Chandrasekhar mass. Eventually, this leads to the initiation of SNe Ia.

Nucleosynthesis in such He shell flashes has been calculated for various set of (M_{WD}, M_{env}) (Nomoto et al. 2013; Shen and Bildsten 2007). For higher maximum temperatures, heavier elements, such as ^{28}Si and ^{32}S, are synthesized. However, the maximum temperature is not high enough to produce ^{40}Ca. After the peak, some amount of He remains unburned in the flash and burns into C+O during the stable He shell burning. In this way, it is possible that interesting amount of intermediate mass elements (IME), including Si and S, already exist in the unburned C+O layer at $M_r \geq 1.2 M_{\odot}$.
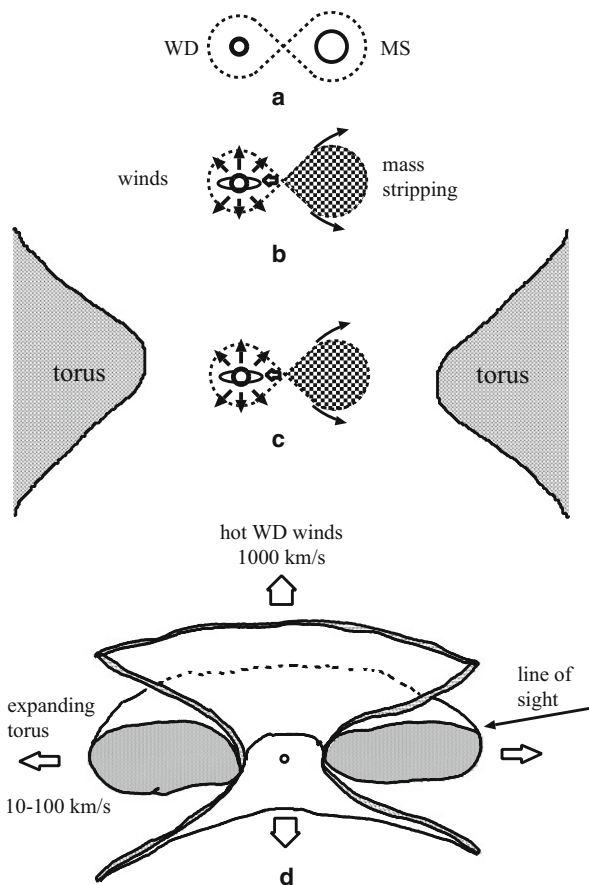
Fig. 2 A schematic configuration of a binary evolution including mass-stripping effect (Hachisu et al. 2008a). (**a**) Here we start a pair of a C+O WD and a more massive main-sequence (*MS*) star with a separation of several to a few tens of solar radii. (**b**) When the secondary evolves to fill its Roche lobe, mass transfer onto the WD begins. The mass transfer rate exceeds a critical rate M_{cr} for optically thick winds. Strong winds blow from the WD. (**c**) The hot wind from the WD hits the secondary and strips off its surface. (**d**) Such stripped-off material forms a massive circumstellar disk or torus and it gradually expands with an outward velocity of $\sim$10–100 km s^{-1}. The interaction between the WD wind and the circumstellar torus forms an hourglass structure. The WD mass increases up to $M_{Ia} = 1.38 \, M_\odot$ and explodes as an SN Ia

2.3 Four Types of Type Ia Supernovae (SNe Ia) in the Single-Degenerate (SD) Scenario

Based on the above properties of accretion-induced hydrogen shell burning, the binary system in the SD scenario evolves through stages (a)–(d) below (also shown in Fig. 2a–d: Hachisu et al. 2008a).

The more massive (primary) component of a binary evolves to a red-giant star (with a helium core) or an AGB star (with a C+O core) and fills its Roche lobe. Mass transfer from the primary to the secondary begins and a common envelope is formed. After the first common envelope evolution, the separation shrinks and the primary component becomes a helium star or a C+O WD. The helium star evolves to a C+O WD after a large part of helium is exhausted by core helium burning. We eventually have a close pair of a C+O WD and a main-sequence (MS) star (Fig. 2a).

Further evolution of the system depends on the binary parameters. Depending on at which stage SNe Ia are triggered, the SD scenario predicts the following four variations of SNe Ia.

2.3.1 SNe Ia-Circumstellar Matter (CSM)

After the secondary evolves to fill its Roche lobe, the mass transfer to the WD begins. This mass transfer occurs on a thermal timescale because the secondary mass is more massive than the WD. The mass transfer rate exceeds $\dot{M}_{cr}$ for the optically thick wind to blow from the WD (Hachisu et al. 1996, 1999a,b) (Fig. 2b).

Optically thick winds from the WD collide with the secondary surface and strip off its surface layer. This mass-stripping attenuates the rate of mass transfer from the secondary to the WD, thus preventing the formation of a common envelope for a more massive secondary in the case with than in the case without this effect. Thus the mass-stripping effect widens the donor mass range of SN Ia progenitors (Fig. 2c).

Such stripped-off matter forms a massive circumstellar torus on the orbital plane, which may be gradually expanding with an outward velocity of $\sim$10–100 km s^{-1} (Fig. 2d), because the escape velocity from the secondary surface to L3 point is $v_{esc} \sim 100$ km s^{-1}. Subsequent interaction between the fast wind from the WD and the very slowly expanding circumbinary torus forms an hourglass structure (Fig. 2c–d). When we observe the SN Ia from a high inclination angle such as denoted by "line of sight," circumstellar matter can be detected as absorption lines like in SN 2006X.

This scenario predicts the presence of several types of circumstellar matter around the binary system, which are characterized various wind velocities v_w: (1) white dwarf winds with such high velocities as $v_w \sim 1000$ km s^{-1}, (2) slow dense matter stripped off the companion star by the white dwarf wind, (3) slow wind matter ejected from a red-giant, and (4) moderate wind velocities blown from the main-sequence star.

The above features are supported by observations of the presence of circumstellar matter in some SNe Ia (Foley et al. 2012; Patat et al. 2007; Sternberg et al. 2011) and the detection of H in circumstellar-interaction-type supernovae (Ia/IIn) such as SN 2002ic (Hamuy et al. 2003). SN 2002ic shows the typical spectral features of SNe Ia near maximum light but also apparent hydrogen features that have been absent in ordinary SNe Ia. Its light curve has been reproduced by the model of interaction between the SN Ia ejecta and the H-rich circumstellar medium (Fig. 3) (Nomoto et al. 2005).
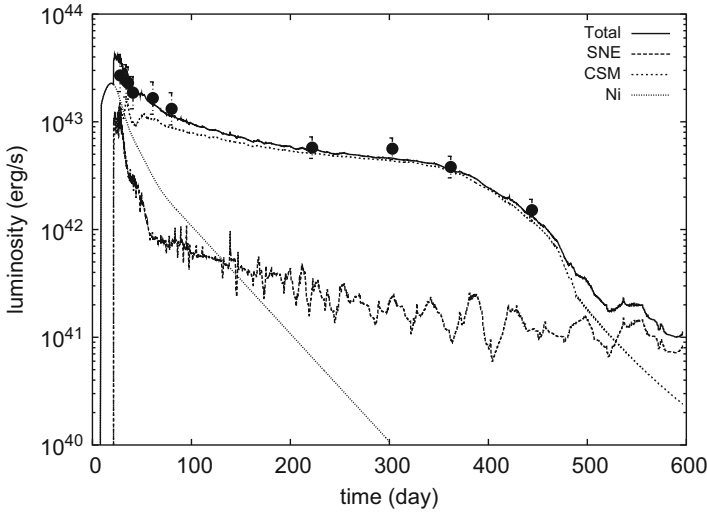
Fig. 3 The observed light curve of SN Ia 2002ic (*filled circles*) and the calculated light curve with circumstellar interaction (Nomoto et al. 2005)

2.3.2 SNe Ia-Supersoft X-Ray Sources (SSXS)

When the mass transfer rate decreases to the following range: $\dot{M}_{\text{stable}} < \dot{M} < \dot{M}_{\text{cr}}$, optically thick winds stop, and the WDs undergo steady H burning. The WDs are observed as supersoft X-ray sources (SSXSs) until the SN Ia explosion. The stripped-off material forms circumstellar matter (CSM) but it has been dispersed too far to be detected immediately after the SN Ia explosion.

2.3.3 SNe Ia-Recurrent Novae (RN)

When the mass transfer rate from the secondary further decreases below the lowest rate of steady hydrogen burning, i.e., $\dot{M}_{\text{transfer}} < \dot{M}_{\text{stable}}$, hydrogen shell burning is unstable to trigger a mild flashes, which recur many times in a short period as a recurrent nova (RN) (e.g., Hachisu and Kato 2001). Its recurrent period is as short as ~ 1 yr, which can be realized for high M and high $\dot{M}$ as discussed in Sect. 2.1. These flashes burn a large enough fraction of accreted hydrogen to increase M to SNe Ia.

Observationally, PTF11kx (Dilday et al. 2012) provides strong evidences that the accreting white dwarf was a recurrent nova and the companion star was a red supergiant.

2.3.4 SNe Ia-He White Dwarf

In the rotating white dwarf scenario, which will be discussed in the later section (e.g., Benvenuto et al. 2015), ignition of central carbon burning is delayed in some cases due to the larger Chandrasekhar mass of the rotating white dwarfs than non-rotating white dwarfs. This delay time after the end of accretion up to the SN Ia

explosion depends on the timescale of angular momentum loss from the C+O white dwarfs and could be long enough for the companion star to evolve into a He white dwarf and for circumstellar materials to disperse. For such a delayed SN Ia, it would be difficult to detect a companion star or circumstellar matter.

2.4   Companion Stars in the SD Scenario

In SD scenario, SNe Ia can occur for a wide range of $\dot{M}$. The progenitor white dwarfs can grow their masses to the Chandrasekhar mass by accreting hydrogen-rich matter at a rate as high as $\dot{M} \gtrsim 10^{-7} - 10^{-6} M_\odot$ yr^{-1} (e.g., Hachisu et al. 1996, 1999a,b; Han and Podsiadlowski 2004; Langer et al. 2000; Li and van den Heuvel 1997; Nomoto et al. 2000b).

Two types of binary systems can provide such high accretion rates, i.e., (1) a white dwarf and a lobe-filling, more massive (up to $\sim 7 M_\odot$), slightly evolved main-sequence or subgiant star (WD + MS) and (2) a white dwarf and a lobe-filling, less-massive (typically $\sim 1 M_\odot$), red-giant (WD + RG) (Hachisu et al. 1999a,b). Figure 4 shows these two regions of (WD + MS) and (WD+RG) in the log $P - M_2$ (orbital period – secondary mass) plane (Hachisu et al. 2008b).

Here the metallicity of $Z = 0.02$ and the initial white dwarf mass of $M_{\mathrm{WD},0} = 1.0 \ M_\odot$ are assumed. The initial system inside the region encircled by a thin solid line (labeled "initial") increases its WD mass up to the critical mass ($M_{\mathrm{Ia}} =$
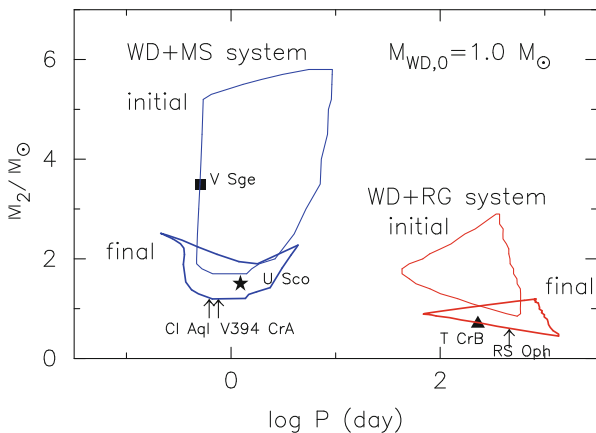

Fig. 4 The regions that produce SNe Ia are plotted in the log $P - M_2$ (orbital period – secondary mass) plane for the (WD + MS) system (*left*) and the (WD + RG) system (*right*) (Hachisu et al. 2008b). Currently known positions of the recurrent novae and supersoft X-ray sources are indicated by a *star mark* ($\star$) for U Sco, a *triangle* for T CrB, a *square* for V Sge, but by *arrows* for the other three recurrent novae, V394 CrA, CI Aql, and RS Oph. Two subclasses of the recurrent novae, the U Sco type and the RS Oph type, correspond to the WD + MS channel and the WD + RG channel of SNe Ia, respectively

1.38 $M_\odot$) for the SN Ia explosion, the regions of which are encircled by a thick solid line (labeled "final").

Note that the "initial" region of WD + MS systems extends up to such a massive ($M_{2,0} \sim 5-6\ M_\odot$) secondary, which consists of a very young population of SNe Ia with such a short delay time as $t \lesssim 0.1$ Gyr. On the other hand, the WD + RG systems with a less massive RG ($M_{2,0} \sim 0.9-1.0\ M_\odot$) consist of a very old population of SNe Ia of $t \gtrsim 10$ Gyr.

Delay time distribution (DTD) of SNe Ia on the basis of the above SD model (Fig. 4) has a featureless power law being in good agreement with the observation (Hachisu et al. 2008b). This is because the mass of the secondary star of the SN Ia system ranges from $M_{2,0} \sim 0.9$ to $6\ M_\odot$ due to the effects of the WD winds and the mass stripping. In our model, moreover, the number ratio of SNe Ia between the WD + MS component and the WD + RG component is $r_{MS/RG} = 1.4$. Such almost equal contributions of the two components help to yield a featureless power law.

2.5 Rotating White Dwarf

2.5.1 Uniform Rotation and Delayed Carbon Ignition

In the above sections, some observations that support the SD scenario are given. However, there has been no direct indication of the presence of companions, e.g., the lack of companion stars in images of SN 2011fe (Li et al. 2011) and some Type Ia supernova remnants (Schaefer and Pagnotta 2012). The rotating white dwarf scenario solves this missing-companion problem (Benvenuto et al. 2015; Di Stefano et al. 2011; Hachisu et al. 2012a; Justham 2011).

The rotating WD evolves as follows Hachisu et al. (2012a) and Benvenuto et al. (2015).

1. For certain ranges of binary parameters, the accretion rate ($\dot{M}$) always exceeds $10^{-7}\ M_\odot\ y^{-1}$ so that the WD increases its mass until it undergoes "prompt" carbon ignition. The mass of the uniformly rotating WD at the carbon ignition, M_{ig}^R, is larger for smaller $\dot{M}$. For $\dot{M} = 10^{-7}\ M_\odot\ y^{-1}$, $M_{ig}^R = 1.43\ M_\odot$, which is the largest mass because nova-like hydrogen flashes prevent the the WD mass from growing for the lower $\dot{M}$. Because of the centrifugal force in the rotating WD, $M_{ig}^R = 1.43\ M_\odot$ is larger than $M_{ig}^{NR} = 1.38\ M_\odot$ (Nomoto et al. 1984).
2. For adjacent ranges of binary parameters, the mass of the rotating WD exceeds $M_{ig}^{NR} = 1.38\ M_\odot$ but does not reach $M_{ig}^R = 1.43\ M_\odot$ because of the decreasing accretion rate. After the accretion rate falls off, the WD undergoes the angular momentum-loss (J-loss) evolution. The exact mechanism and the time scale of the J-loss are highly uncertain, although the magneto-dipole braking WD is responsible. J-loss induces the contraction of the WD, which leads to the "delayed" carbon ignition after the "delay" time due to neutrino and radiative cooling.
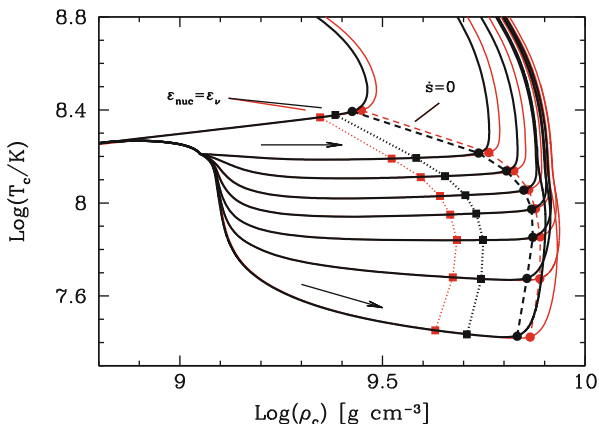
Fig. 5 The evolutionary tracks of the center of the WD up to the onset of the hydrodynamical explosion (Benvenuto et al. 2015). $\varepsilon_{nuc} = \varepsilon_\nu$ indicates the conditions at which neutrino losses equal nuclear energy release, while $\dot{S} = 0$ show the stages at which central entropy per baryon begins to increase. *Thick black* and *thin red lines* correspond to the treatments of screening given by Kitamura (2000) and Potekhin and Chabrier (2012), respectively. *Arrows* indicate the sense of the evolution

Figure 5 shows the evolution of the center of the WD since before the end of accretion up to the onset of the hydrodynamical stage (Benvenuto et al. 2015). The uppermost line corresponds to the case (1) evolution that leads to the "prompt" carbon ignition. Below that, the lines from upper to lower correspond to the evolutions with increasing J-loss timescale ($\tau_J = 1, 3, 10, 30, 100, 300,$ and 1000 Myr, respectively) that lead to the "delayed" carbon ignition.

In what binary systems (P and M_2) the uniformly rotating WD undergoes the delayed carbon ignition? The result for the initial WD masses of 0.9 $M_\odot$ is shown in Fig. 6. Here the binary systems starting from the "painted" region of the ($P - M_2$) plane reach 1.38 $M_\odot < M < 1.43 M_\odot$, while the systems starting from the blank region encircled by the solid line reach $M = 1.43 M_\odot$. The occurrence frequency of the delayed carbon ignition would roughly be one-third of the total frequency of the carbon ignition.

For the values of τ_J considered here, the WD spends a time to undergo SN Ia explosion enough for the donor star to evolve to a structure completely different from the one it had when acted as a donor. For the red-giant donor, its H-rich envelope would be lost as a result of H-shell burning and mass loss so that it would become a He WD in ∼10 Myr. For the main-sequence donor, it would also evolve to become a low mass He WD in 1 Myr, a hot He WD in 10 Myr, and a cold He WD in 1000 Myr (Di Stefano et al. 2011). So, the J-losses should delay the explosion a time enough for the former donor to be undetectable. Therefore, this scenario provides a way to account for the failure in detecting companions to SNe Ia.

Such He white dwarf companions would be faint enough not to be seen before or after the Type Ia supernova explosion. This new single-degenerate scenario can
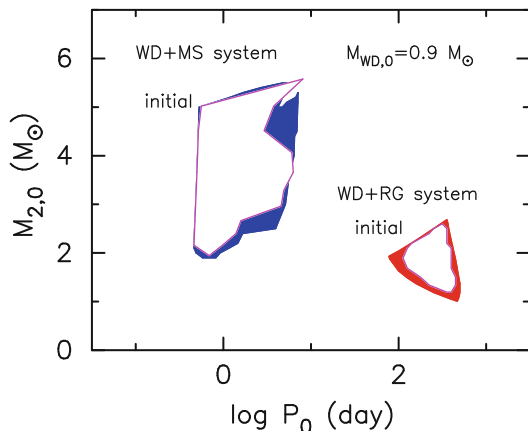
Fig. 6 The outcome of the binary evolution of the WD + companion star systems is shown in the parameter space of the initial orbital period P and the companion mass M_2 for the initial WD mass of $0.9\,M_\odot$ (Benvenuto et al. 2015). The mass M of the WD starting from the "painted" region reaches $1.38\,M_\odot < M < 1.43\,M_\odot$ (delayed carbon ignition), while the systems starting from the blank region encircled by the *solid line* reach $M = 1.43\,M_\odot$ (prompt carbon ignition)

explain in a unified manner why no signatures of the companion star are seen in some Type Ia supernovae, whereas some Type Ia supernovae indicate the presence of the companion star.

2.5.2 Differential Rotation and Super-Chandra SNe Ia

If the accretion leads to nonuniform, differentially rotating WDs, carbon ignition occurs at super-Chandrasekhar masses (Hachisu et al. 2012b). The WD mass can increase by accretion up to 2.3 (2.7) $M_\odot$ from the initial value of 1.1 (1.2) $M_\odot$, being consistent with high luminosity SNe Ia such as SN 2003fg, SN 2006gz, SN 2007if, and SN 2009dc (Kamiya et al. 2012). Such very bright super-Chandrasekhar mass SNe Ia are suggested to born in a low metallicity environment.

3   One-Dimensional Explosion Models of Chandrasekhar Mass White Dwarfs

In the Chandrasekhar mass models, carbon burning ignited in the central region is unstable to flash because of strong electron degeneracy and release a large amount of nuclear energy explosively. However, the central density is too high, and thus the shock wave is too weak to initiate spontaneously a carbon detonation (because of temperature-insensitive pressure of strongly degenerate electrons).

Then the explosive thermonuclear burning front propagates outward as a convective deflagration wave (subsonic flame) (e.g., Arnett 1996; Nomoto et al. 1984).

Rayleigh-Taylor instabilities at the flame front cause the development of turbulent eddies, which increase the flame surface area, enhancing the net burning rate and accelerating the flame. In the 1D convective deflagration model W7 (Nomoto et al. 1984), the flame speed is prescribed by time-dependent mixing-length theory with the mixing length being 0.7 of the pressure scale height. In some cases the deflagration may undergo "deflagration to detonation transition (DDT)" (Khokhlov 1991). In the 1D DDT model WDD2 (Iwamoto et al. 1999), DDT is assumed to occur when the density at the flame front decreases to $2 \times 10^7 \, \mathrm{g \, cm^{-3}}$. Such a turbulent nature of the flame propagation has been studied in multidimensional simulations as will be described in the subsequent sections (Hillebrandt and Niemeyer 2000).

3.1   Nucleosynthesis in Deflagration and Detonation

In this section, we use 1D hydrodynamical models W7 and WDD2 to summarize the products of explosive nucleosynthesis which takes place behind the deflagration-detonation wave. Figures 7 and 8 show the isotopic distributions as a function of the enclosed mass for W7 (Nomoto et al. 1984; Mori et al. 2016) and WDD2 (Iwamoto et al. 1999; Mori et al. 2016).

In the inner core of W7, the temperature behind the deflagration wave exceeds $\sim 5 \times 10^9 \, \mathrm{K}$, so that the reactions are rapid enough (compared with the expansion timescale) to realize nuclear statistical equilibrium (NSE), thus synthesizing Fe-peak elements, mainly $^{56}\mathrm{Ni}$ of 0.65 $M_\odot$ (Nomoto et al. 1984; Mori et al. 2016). The surrounding layers gradually expand during the subsonic flame propagation, so that the densities and temperatures get lower. As a result, explosive burning produces the intermediate mass elements Si, S, Ar, and Ca due to lower peak temperatures than in the central region. In WDD2, the flame speed is assumed to be slower than W7 so that the mass of the materials undergoing deflagration is smaller. Instead, the detonation produces $^{56}\mathrm{Ni}$ and Si, S, Ar, and Ca in the outer layers. The total amount of $^{56}\mathrm{Ni}$ is 0.67 $M_\odot$ (Iwamoto et al. 1999; Mori et al. 2016).

In these Chandrasekhar mass models, the central densities of the WDs are so high ($3 \times 10^9 \, \mathrm{g \, cm^{-3}}$ for W7 and WDD2) that the Fermi energy of electrons tends to exceed the energy thresholds of the electron captures involved. Electron captures reduce the electron mole fraction, Y_e, that is the number of electrons per baryon. As a result of electron capture, the Chandrasekhar mass model synthesizes a significant amount of neutron-rich species, such as $^{58}\mathrm{Ni}$, $^{56}\mathrm{Fe}$, $^{54}\mathrm{Fe}$, and $^{55}\mathrm{Mn}$. Figures 9 and 10 show the abundance ratios of the integrated amount of species relative to $^{56}\mathrm{Fe}$ with respect to the solar abundance ratio. It is seen that some neutron-rich species are enhanced relative to $^{56}\mathrm{Fe}$.

The detailed abundance ratios with respect to $^{56}\mathrm{Fe}$ depends on the convective flame speed and the central densities and also the weak reaction rates. In Figs. 7 and 8, the most updated weak reaction rates are applied for electron capture (Mori et al. 2016).
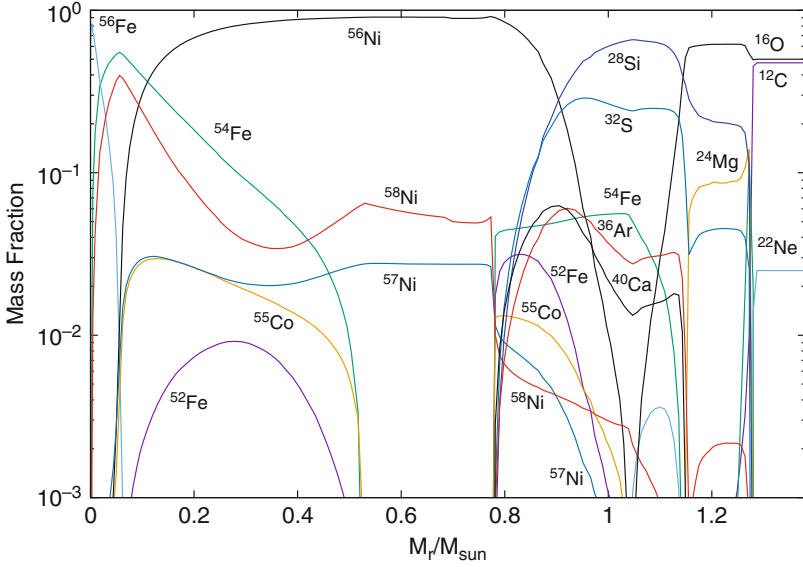
Fig. 7 Isotopic distributions as a function of the enclosed mass for the deflagration model W7 (Nomoto et al. 1984; Mori et al. 2016). Here the most updated weak reaction rates are applied (Mori et al. 2016)
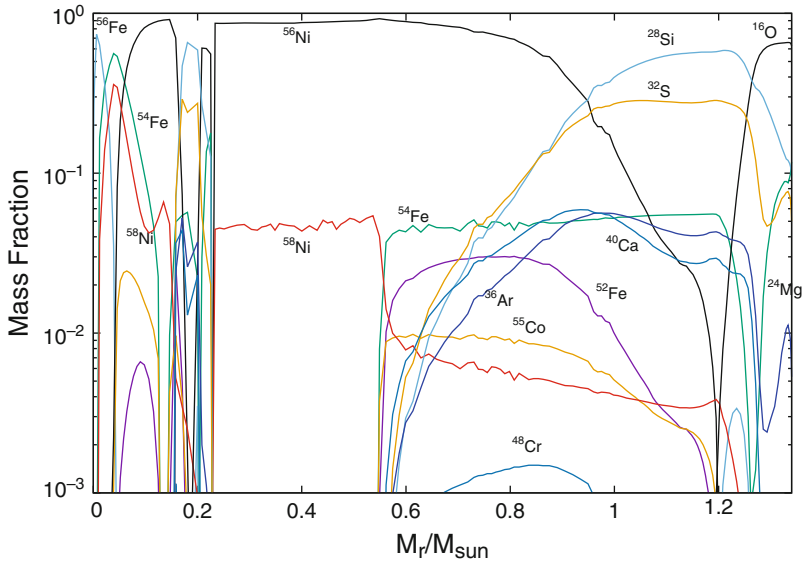

Fig. 8 Same as Fig. 7, but for the DDT model of WDD2 (Iwamoto et al. 1999; Mori et al. 2016). Here the most updated weak reaction rates are applied (Mori et al. 2016)
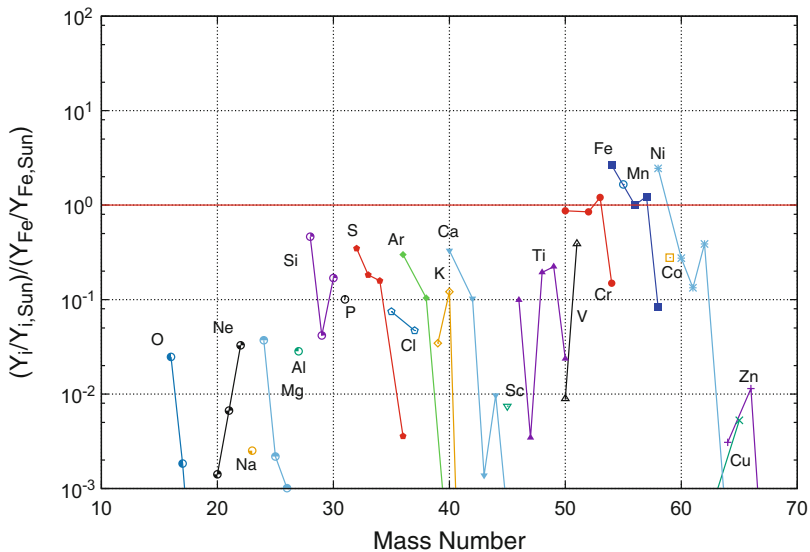
Fig. 9 The abundance ratios of the integrated amount of stable isotopes relative to ^{56}Fe with respect to the solar abundance ratio for the deflagration model W7 shown in Fig. 7 (Nomoto et al. 1984; Mori et al. 2016)
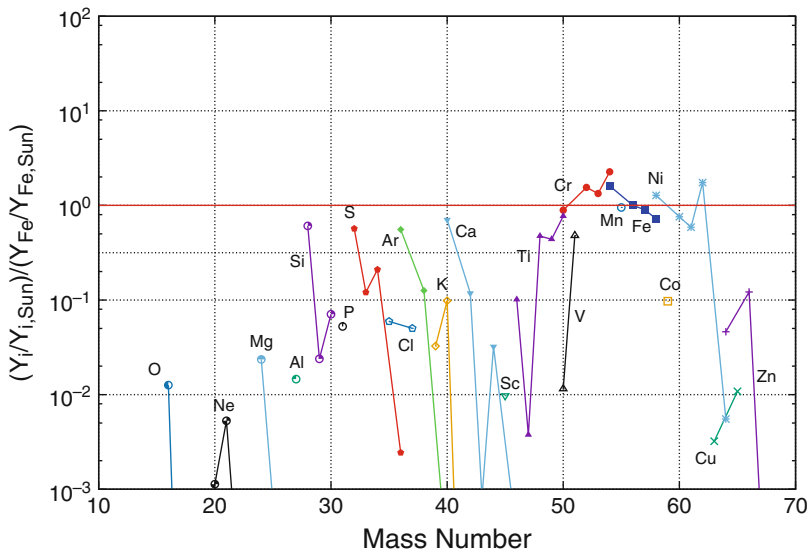

Fig. 10 Same as Fig. 9, but for the DDT model of WDD2 (Iwamoto et al. 1999; Mori et al. 2016)

It is also important to note that the synthesized amounts of neutron-rich species (^{58}Ni, ^{56}Fe, ^{54}Fe, and ^{55}Mn) differ between the Chandra and sub-Chandra models because of the difference in the central densities of the WDs (Yamaguchi et al. 2015).

3.2 Observable Characteristics of Chandrasekhar Mass Models

The main observable characteristics of SNe Ia are their optical light curves and spectra. The light curves are powered primarily via the decays of ^{56}Ni and its daughter ^{56}Co. The early spectra are characterized by the presence of strong absorption lines of Si as well as lines from intermediate mass elements such as Ca, S, Mg, and O as well as the Fe-peak elements Fe, Ni, and Co as seen in Fig. 11 (Krause et al. 1997). The late-time spectra show emission lines of Fe-peak elements, which include those of stable Ni, i.e., neutron-rich ^{58}Ni. It is thus evident that the light curves and spectra are closely related to the nucleosynthesis, which is crucial to study the unresolved issues regarding the explosion models and the progenitors of SNe Ia.
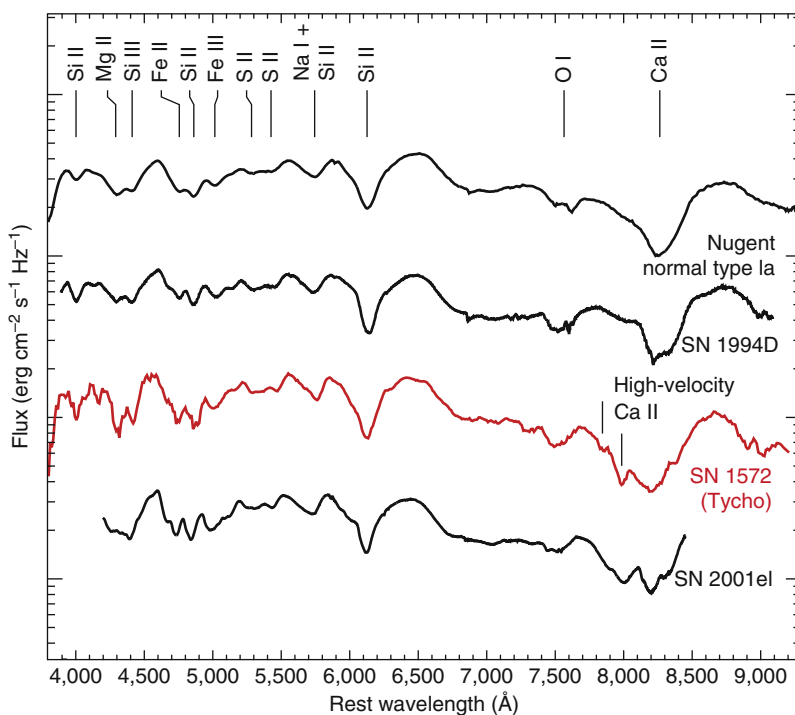

Fig. 11 Observed spectra at near maximum light of several Type Ia supernovae, including Tycho's supernova 1572, with the line identifications of several elements (Krause et al. 1997)

Fig. 12 Comparison between the observed spectra of Type Ia supernova (SN 1994D at maximum light and SN 1992A at 5 days after maximum light) with the synthetic spectra of the carbon deflagration model W7 at 20 days and 23 days after the explosion, respectively (Nugent et al. 2000)
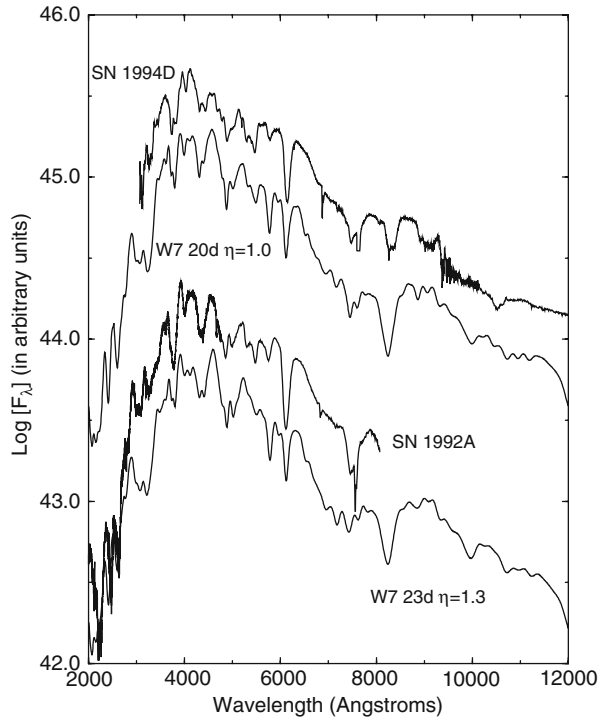
Both W7 and WDD2 models are successful in reproducing the basic features of SN Ia light curves and spectra near maximum light as seen from the synthetic spectra of W7 in Fig. 12 (Nugent et al. 2000). Important point is that the subsonic deflagration decreases the densities of the Chandrasekhar mass WD before the deflagration or detonative wave arrives, which is necessary to synthesize enough amount of intermediate mass elements (Ca, S, Si, Mg, and O) rather than to incinerate most of C+O into NSE (Fe-peak elements) (Arnett 1969).

This demonstrates the important roles of 1D hydrodynamical models even these are approximate: thermonuclear explosion models of WDs work to explain the basic features of "typical" SNe Ia as far as those models form the abundance distributions like W7 and WDD2. Clarifying how those abundance distributions are actually realized is the task of multi-dimensional simulations as will be described in the next sections.

4   Multi-Dimensional Models and Diversity of Explosion Mechanisms

As discussed with 1D hydrodynamical simulations, carbon burning in the center grows into deflagration and detonation. To understand these processes, we

summarize two-dimensional hydrodynamical simulations of the explosion phase
of a carbon-oxygen white dwarf carried out by Leung and Nomoto (2017b).
The hydrodynamics code is extended from the prototype for modeling supernova
explosion (Leung et al. 2015a), which has been used to model subluminous SNe Ia
(Leung et al. 2015b) and Chandrasekhar Mass SNe Ia (Leung and Nomoto 2017a).
It uses the weighted essentially non-oscillatory (WENO) fifth-order scheme for
spatial discretization and the five-step, third-order, non-strong stability-preserving
Runge-Kutta scheme for time discretization. The Helmholtz equation of state is
used to describe the microphysics, which contains an ideal degenerate electron
gas at any relativistic level, a classical ideal gas of ions, a photon gas assuming
Planck distribution and electron-positron pair. The screening of electron gas is
included. To describe the explosion, the level set is applied to track both the fronts
of deflagration and detonation. The energy release assumes a three-step scheme, the
carbon burning, burning toward the nuclear quasi-statistical equilibrium (NSE) and
burning toward NSE.

The seven-isotope network containing ^{4}He, ^{12}C, ^{16}O, ^{20}Ne, ^{24}Mg, ^{28}Si, and ^{56}Ni
is used to describe the chemical composition of matter. To determine the propagation
of deflagration, the turbulent flame speed formula (Pocheau 1994; Schmidt et al.
2006) is used with the one-equation model for the evolution of turbulence. For the
detonation speed and its energy production, the pathological detonation is assumed
as described in details in the Appendix. For models with DDT transition, detonation
is triggered when locally Ka = 1 is satisfied.

4.1   Deflagration-Detonation Transition (DDT) Model

The deflagration-detonation transition (DDT) model (Khokhlov 1991) combines
the slow burning phase at the beginning and the rapid explosion phase afterward,
which provides sufficient time for electron capture, and ensures most of the fuel, in
the form of carbon-oxygen mixture, is burnt before the WD expansion ceases the
nuclear reaction (Iwamoto et al. 1999).

Figure 13 shows the temperature color-plot for the turbulent deflagration with
DDT in a typical SNe Ia model. For the WD, the central density of $3 \times 10^9 \, \mathrm{g\,cm^{-3}}$
with an isothermal profile of 10^8 K is assumed. The composition is assumed to be at
solar metallicity with $X(^{12}\mathrm{C})/X(^{16}\mathrm{O}) = 1$ by mass. The turbulent flame allows
the flame to propagate quickly before the Rayleigh-Taylor instabilities become
important. This ensures that sufficient amount of matter is burnt before the density
of flame front is low enough to trigger detonation. The typical temperature in the
deflagration zone is around 5×10^9 K at the time when detonation is commenced.
Owing to the low-density fuel, the temperature in the ash made by detonation is
comparably lower, at 3×10^9 K. Due to the correlated shock, hot spots can be found
when the high-velocity flow collides with the boundary, which can be as high as
7×10^9 K. However, this feature might not appear so frequently in three-dimensional
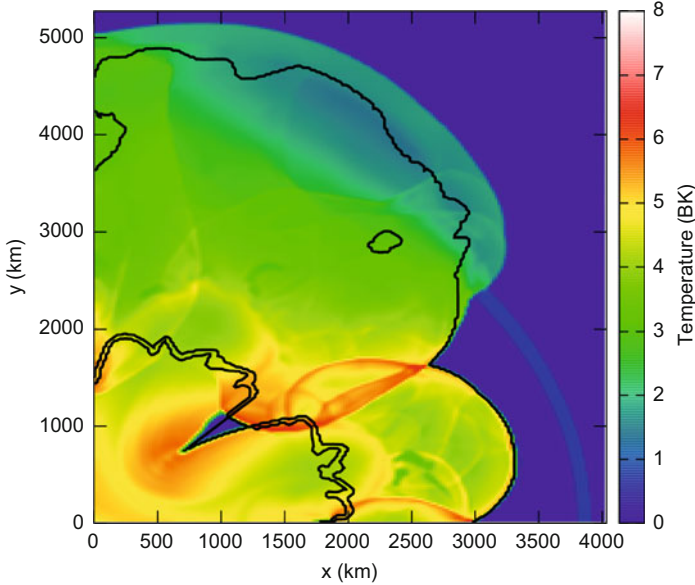simulations because of the lower degree of symmetry.

Fig. 13 The temperature color-plot of the turbulent deflagration model with DDT at about 0.4 s after DDT is triggered (Leung and Nomoto 2017b). The *solid lines* stand for the shape of the deflagration and detonation front. The central density is set at $3 \times 10^9 \, \mathrm{g \, cm^{-3}}$ with isothermal profile of 10^8 K. The composition is assumed to be at solar metallicity with $X(^{12}C)/X(^{16}O) = 1$ by mass. The $c3$ flame is chosen as the initial flame

Fig. 14 The chemical abundance of the typical SNe Ia using the DDT model presented in Fig. 22 (Leung and Nomoto 2017b). The ratio is $[X/X(^{56}Fe)]/[X/X(^{56}Fe)]_\odot$. The two lines stand for the typical uncertain range of a factor of 2

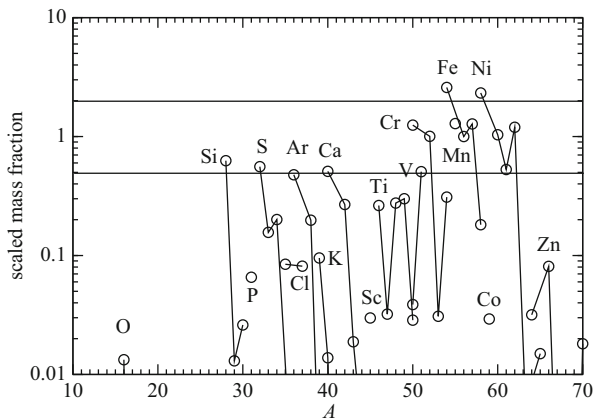Figure 14 shows the chemical abundance of the DDT model by calculating nucleosynthesis using the tracer particles data. In the SN Ia simulation, due to the heavy computation of multidimensional hydrodynamics, the large nuclear reaction network is used for a post-process, where the thermodynamics trajectories of the massless particles are used only to follow the fluid advection without affecting

the hydrodynamics. In the hydrodynamics, only the simplest network can capture the essence of deflagration and detonation to reduce the workload in isotope advection. With those two networks, reasonably accurate energy production in the hydrodynamics and a detailed nucleosynthesis structure can be obtained. Almost all $C + O$ fuel is consumed; thus, only a trace of ^{16}O is left behind. On the contrary, other α-chain isotopes, such as ^{28}Si, ^{32}S, ^{36}Ar, and ^{40}Ca, are very close to the solar abundance. The isotopes with an odd atomic number is always under-produced as expected. Most iron-peak elements, such as chromium, iron, manganese, and nickel, are mostly consistent with solar abundance, with a slight overproduction of ^{54}Fe and ^{58}Ni.

4.2 Pure Turbulent Deflagration (PTD) Model

The 2D pure deflagration model has its theoretical weakness in terms of significant unburnt material at the core. However, with the rapidly growing observation data of supernovae, some peculiar SNe Ia whose explosion observables are incompatible with the standard picture can be explained by this model.

4.2.1 Weak Explosion

Theoretically, flame has been suggested to fail to develop into detonation in the following two cases. First possibility is the hybrid white dwarf with a $C + O$ core and an O+Ne envelope. This type of white dwarf has been suggested to be originated from a main-sequence star around $10\,M_\odot$. In the main-sequence star evolution, a C+O core of mass $\sim 0.6 - 1.0\,M_\odot$ is formed. When the inner core cools down and contracts, the the surface of the carbon-oxygen core can be hot enough to carry out carbon burning. In the standard picture, the burning appears in the form of flame, which gradually propagates inward due to thermal diffusion. At the end, the flame reaches the center such that the core becomes carbon-free. However, whether the carbon flame can spread from the core surface to the center depends strongly on the convective boundary mixing (Denissenkov et al. 2013).

This is a poorly known quantity due to its multidimensional nature. Within the theoretical uncertainties, the carbon flame can be stopped, leaving a small carbon-oxygen core and a neon-oxygen envelope.

Second, the model is the same as the typical explosion by a carbon-oxygen white dwarf, but without detonation transition. Notice that whether or not the detonation can start is still a matter under debate. In general it requires certain mechanism, for example, turbulent diffusion, in order to create a temperature gradient which allows supersonic burning as suggested by Zel'dovich gradient mechanism. In fact, whether turbulence can or cannot provide the required diffusion to smear out the flame is uncertain due to the lack of required resolution for resolving the heat diffusion around the flame surface. As a result, in another limit, it is possible that the explosion develops as pure turbulent flame without any transition (Fink et al. 2014).

In all cases, the flame ceases to develop into detonation even when the flame has reached the distributed burning regime. As a result, with the energy from the
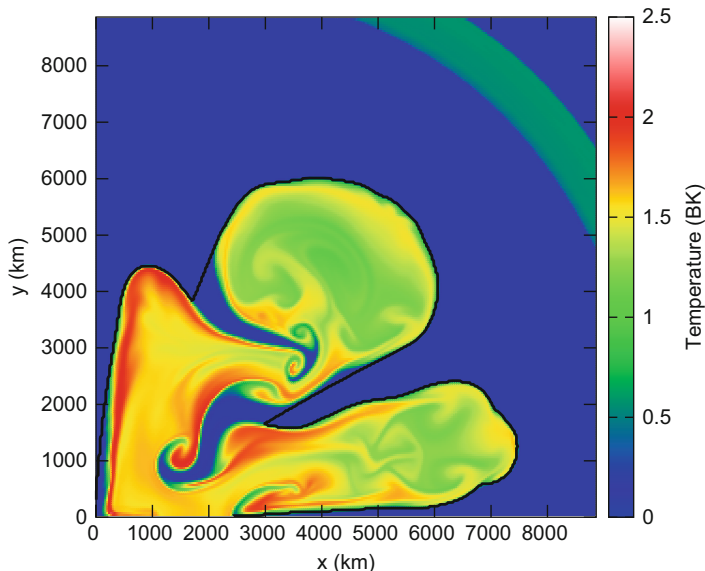
Fig. 15 The temperature color-plot of a SN Ia model using the pure turbulent deflagration model at time ≈ 1.3 s (Leung and Nomoto 2017b). The *solid lines* stand for the shape of the deflagration. The central density is set at 3×10^9 g/cm^3 with isothermal profile of 10^8 K. The composition is assumed to be at solar metallicity with $X(^{12}\text{C})/X(^{16}\text{O}) = 1$ by mass. An initial $c3$ flame is patched as to bypass the slow simmering phase

carbon deflagration only, the star is barely unbound. This means the ejecta mass is much lower than usual SNe Ia. And the ejecta velocity is also much lower. Without detonation, the iron-production is much lower than typical SNe Ia. The corresponding isotope ratio of those iron-peaked elements will be much higher. In observations, this type of objects show a very transient and dim signal. The light curve is much different from those of usual SNe Ia. With a low ^{56}Ni production, the peak luminosity can be lower by 2–5 by absolute magnitude and shows no secondary maximum due to turbulent mixing. The optical signal is also viewing-angle dependent that preserves moderately the anisotropy of the flame. The model has been applied to explain the prototypical SN Iax 2002cx (Kromer et al. 2013) and the dimmest SN Iax 2008ha (Kromer et al. 2015).

Figure 15 shows the flame structure of one of the realization using the pure turbulent deflagration model (Leung and Nomoto 2017b). The model is chosen to be typical for SNe Ia, with a central density of 3×10^9 g cm^{-3} and an isothermal profile of 10^8 K. The composition is assumed to be at solar metallicity with $X(^{12}\text{C})/X(^{16}\text{O}) = 1$ by mass. At about 1 s after the flame has started, the energy release is mostly finished. The flame preserve the initial three-finger structure. The large-scale Rayleigh-Taylor instability is enhanced, showing injection of cold fuel into ash between the "fingers." Furthermore, curly shape appears along the finger structure, which demonstrates the Kelvin-Helmholtz instabilities perturbing

Fig. 16 The chemical abundance $[X/X(^{56}\text{Fe})]/[X/X(^{56}\text{Fe})]_{\odot}$ of the typical SN Ia using the PTD model. The two lines stand for the typical uncertain range of a factor of 2
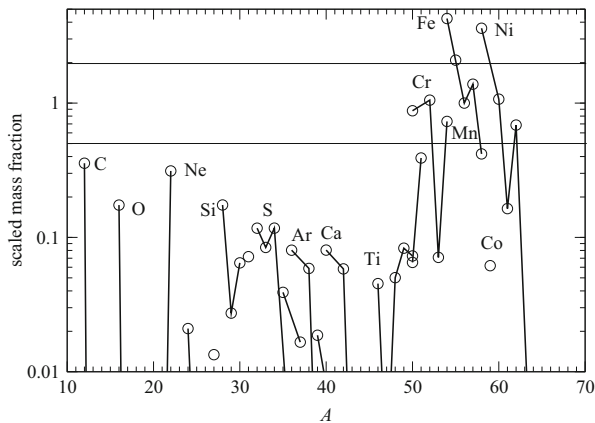
the flame surface. The outer atmosphere is mildly heated up due to the expansion of the inner matter.

Figure 16 shows the chemical composition of the pure turbulent deflagration (PTD) model (Leung and Nomoto 2017b) similar to Fig. 14. Without the detonation, most of the low-density material remains unburnt. As a result there is a significant amount of ^{12}C and ^{16}O. ^{20}Ne, which is a product of deflagration at low-density is largely preserved. However, due to the slow propagation of flame at density $\sim 10^7 \,\text{g cm}^{-3}$, most intermediate mass elements (IME) is under-produced. The iron-peak elements, in general, are well produced. Since the ratio is taken against ^{56}Fe, where in the PTD model a smaller amount is produced, the overproduction of ^{54}Fe and ^{58}Ni become more severe, even when their net value is closed to the DDT case. Comparing with Fig. 16, it can be seen that most iron-peak elements are produced during the deflagration phase, while the IME are produced by detonation. Notice that there is no clear cut for which elements are solely produced by deflagration and detonation, especially near the deflagration-detonation transition. Compression and expansion due to shock interaction can for example create iron-peak elements in the detonation region. Furthermore, due to the asymmetric structure of the flame, some high-density fuel can be burnt by detonation instead of deflagration, which creates a significant amount of ^{56}Ni.

The upper panel of Fig. 17 shows the luminosity against time for the hybrid WD model (Leung and Nomoto 2017b). The initial stellar model is the same as the PTD and DDT model, which is a WD at $3 \times 10^9 \,\text{g cm}^{-3}$, isothermal profile at 10^8 K. But the chemical composition is different. It has an inner core of $X(^{12}\text{C}) = 0.49$, $X(^{12}\text{O}) = 0.49$, and $X(^{22}\text{Ne}) = 0.02$; the inner envelope of $X(^{12}\text{C}) = 0.03$. $X(^{16}\text{O}) = 0.49$, $X(^{20}\text{Ne}) = 0.46$, and $X(^{22}\text{Ne}) = 0.02$; and an outer envelope with the same composition as the core. To compare the difference in the burning energetic, we also include the results from the PTD and the DDT model.

For the hybrid WD, the carbon deflagration stops once the flame reach the interface. The luminosity drops at $t = 0.8$ s. Owing to the slower burning toward
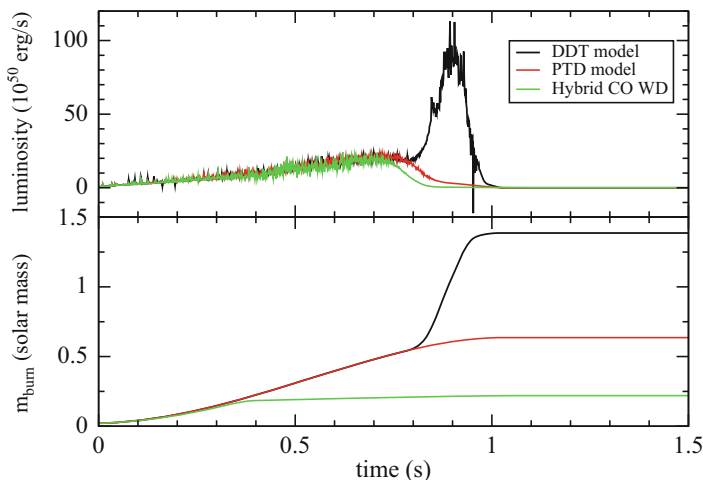
Fig. 17 Panel: The luminosity against time for the hybrid WD model with an ONe envelop in one of the realization (Leung and Nomoto 2017b). The central density is chosen to be $3 \times 10^9 \, \text{g cm}^{-3}$ with an isothermal profile at $10^8 \, \text{K}$. A $c3$ flame is patched to trigger the deflagration phase. For comparison, those of the PTD model and the DDT model are shown

NQSE and NSE, together with the α-recombination during the expansion, the luminosity is observable until $t = 0.9 \, \text{s}$. In both PTD and DDT models, there is no such limit and thus the burning can last for about 1 s. Certainly, a sharp peak in the DDT model demonstrates the powerful energy release in the detonation phase. In the lower panel, we plot similar to the upper panel but for the burnt mass. Coinciding with the luminosity evolution, the hybrid WD model stops its burning at $t = 1.0 \, \text{s}$, showing that only the CO core is consumed. On the contrary, the PTD model can burn about $0.6 \, M_\odot$ at the end of simulation, while the DDT model can burn all the material before the rapid expansion.

Figure 18 shows the energy evolution for the hybrid WD model (Leung and Nomoto 2017b). The total energy reaches its equilibrium value at $t \approx 0.8 \, \text{s}$. Also, it is only slightly above zero, which suggests that the star is barely unbound by the deflagration. The kinetic energy grows slowly in the beginning, since nuclear energy is released in the form of the internal energy. Around $t \approx 0.8 \, \text{s}$, it increases faster and reaches its equilibrium at $t \approx 1 \, \text{s}$. Notice that the continuing growth of the kinetic energy means that the hot matter continues to do work on the expanding matter toward the atmosphere.

Figure 19 shows the ratios of $[X/X(^{56}\text{Fe})]/[X/X(^{56}\text{Fe})]_\odot$ in this type of SN Ia (Leung and Nomoto 2017b). As expected, the suppression of detonation and the suspension of deflagration in the outer envelope reduce the production of many isotopes. The iron-peak elements such as ^{54}Fe and ^{58}Ni, which are mostly produced by detonation, are significantly enhanced relative to ^{56}Fe. The intermediate mass elements along the α-chain such as ^{28}Si, ^{32}S, and ^{36}Ar are under-produced because they are primarily made by detonation in the region of lower density ($\sim 10^7 \, \text{g cm}^{-3}$).
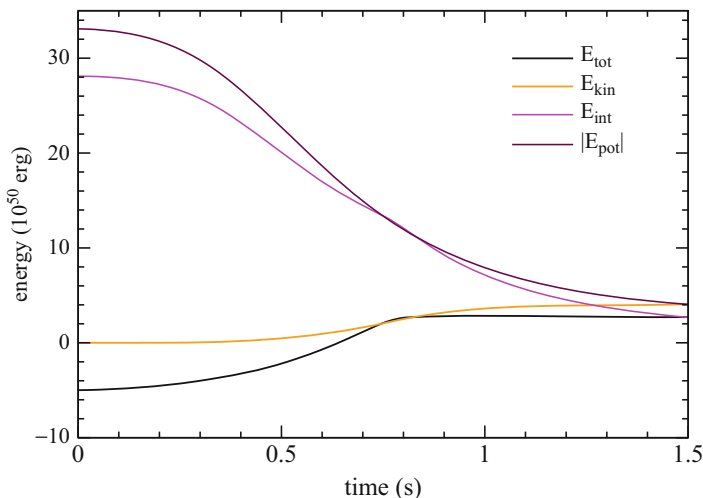
Fig. 18 The time evolution of the total, kinetic, internal and potential energy of the same model as in Fig. 17 (Leung and Nomoto 2017b)
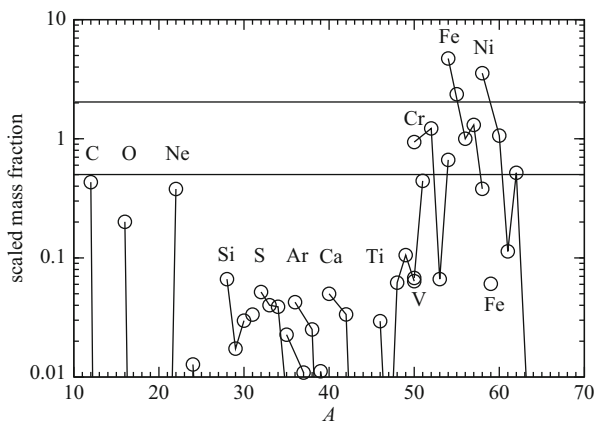

Fig. 19 The chemical abundance ratios $[X/X(^{56}\mathrm{Fe})]/[X/X(^{56}\mathrm{Fe})]_\odot$ of the hybrid WD model for an SN Ia presented in Fig. 18 (Leung and Nomoto 2017b)

4.2.2 Failed Explosion

For a binary system with massive WD ($> 1.2\,M_\odot$), the ignition density is much higher than standard SNe Ia that the released energy cannot unbind the star owing to the efficient energy loss by neutrino and also electron capture. This is also known as the accretion-induced collapse. For an ONeMg WD, the typical ignition density ($\approx 10^{9.95}\,\mathrm{g\,cm^{-3}}$) is higher than that of CO WD ($\approx 2 \times 10^9\,\mathrm{g\,cm^{-3}}$) (Nomoto and Kondo 1991; Schwab et al. 2015). The energy released during deflagration is much smaller than its CO counterpart due to its higher initial binding energy. The high

density also makes the electron capture rate more efficient than that in CO WD. Notice that the majority of WD pressure comes from the electron gas. Due to weak interaction, the reaction $e + p \rightarrow n + \nu_e$ occurs. In particular, for burnt matter with temperature high enough to reach NSE, it contains a significant amount of iron-peaked elements, in which high-Ye isotopes tend to interact with the surrounding electron to form low-Ye but stabler isotopes. The reduction of the electron fraction can significantly lower the pressure, even when its temperature has been raised to $\approx 10^{10}$ K. Furthermore, at this density range, matter is almost transparent to neutrino. The neutrino product can most likely escape from the star without interacting with matter or disposing energy. Therefore, it serves as another source of energy loss. Both factors can considerably lower the pressure of the burnt matter, which stops the flame propagation. The central density increases as a result. Notice that when the density increases, the equilibrium value of Y_e (the value where the beta decay balances the electron capture) decreases. It thus further decreases the pressure in the burnt region and triggers an inward matter flow. The induced gravitational collapse results in a neutron star. After the bounce shock has formed when the matter in the core reaches nuclear density, the bounce shock once stalls outside the neutron star, heat is lost by its own neutrino emission. The stalled shock revived again by the energy deposition from neutrino emitted from the neutron star. As a result, the shock ejects the low-density matter in the envelope and the accretion disk (Kitaura et al. 2006).

4.3   Gravitationally Confined Detonation Model

Another direction for the SNe Ia is the gravitationally confined detonation model (Plewa 2007). It is unclear from the first principle whether turbulence at such high density and high Reynolds number behaves as observed in terrestrial experiments. In another extreme, a flame can be completely unperturbed by the local eddy motion and only subject to large-scale hydrodynamic instabilities, such as the Rayleigh-Taylor instability. In that case, the deflagration propagates in a laminar flame speed, which leads to a small amount of mass being burnt ($\approx 0.1\, M_\odot$) before the flame quenches. Therefore, the burnt matter cannot drive efficiently the matter flow to create detonation spontaneously. Instead, the hot matter flows to the surface and expands. After some time, the hot matter converges again at the point opposite to where it rises at the beginning and sinks. Due to gravitational attraction, the downward flow accumulates and compresses the matter below, which heats up the matter. Once the matter is hot enough to burn carbon, the increased thermal pressure further provides the pressure force to create an ingoing jet, which becomes the seed for the first detonation.

This type of explosion is in general stronger than DDT model because most matter is not burnt in the deflagration phase. Due to the rapid expansion after detonation, most matter preserve a high-Ye value. Also, because of the supersonic propagation of the detonation wave, matter does not have sufficient time to mix before they are ejected. So, the ejecta show a clear stratified structure in the core,

despite that on the surface there could be a trace of the deflagration ash. Because a considerable amount of ^{56}Ni is produced, the model has been applied to explain luminous SNe Ia such as SN 1991T. However, the synthetic spectra cannot match well owing to the strong viewing angle dependence and the strong calcium, silicon, and sulfur lines, which are unobserved in SN 1991T (Seitenzahl et al. 2016).

5   Discussion

5.1   Spectral Diagnostics of Nucleosynthesis

We have discussed many current models and the implementation techniques in previous sections. The hydrodynamics simulation and corresponding nucleosynthesis can be applied to observations through chemical abundances. Through the use of tracer particles, the thermodynamics trajectories of individual fluid parcels can be traced. This provides the necessary data for tracing the nuclear reactions. As one example, we apply such an approach to the Chandra vs. sub-Chandra issue.

For nucleosynthesis yields, whether the explosion is Chandra or sub-Chandra is crucial, because the central density of the white dwarf affects the abundance ratio of Fe-peak elements. Both Chandra and sub-Chandra explosion models can synthesize relevant amounts of ^{56}Ni for Type Ia supernovae (Hillebrandt and Niemeyer 2000). However, the amount of other Fe-peak elements differs, because the ignition density is different: The density can be as high as $>10^9 \, \mathrm{g \, cm^{-3}}$ in the Chandra model whereas as low as $\sim10^7 \, \mathrm{g \, cm^{-3}}$ in the sub-Chandra model.

In the Chandra model, the thermonuclear runaway starts with the ignition of deflagration (Nomoto et al. 1976, 1984). In the high-temperature and high-density bubble, materials are incinerated into nuclear statistical equilibrium and undergo electron capture. Electron capture by free protons and Fe-peak elements leads to the synthesis of ^{58}Ni, ^{54}Fe, and ^{56}Fe (not via ^{56}Ni decay). These neutron-rich Fe-peak elements form a hole that is almost empty of ^{56}Ni (e.g. Nomoto et al. 1984).

In the sub-Chandra model, the ignition density is too low for electron capture to take place. The neutron excess is produced only by the initial CNO elements, which are converted to ^{14}N and to ^{22}Ne. Thus, this excess also depends on the initial metallicity. As a result, ^{58}Ni is almost uniformly distributed with a mass fraction as small as ~0.01 (e.g., Shigeyama et al. 1992). Such differences in the mass and the distribution of ^{58}Ni can be observationally investigated by late-phase (~1 year since the explosion) spectroscopy at near-infrared wavelengths Hillebrandt and Niemeyer 2000). Because ejecta become optically thin at late times, spectroscopy provides an unbiased, direct view of the innermost regions.

Optical observations have shown [FeII] λ 7155 and [NiII] λ 7378 for several SNe Ia (Maeda et al. 2010). The [NiII] λ 7378 line is emitted from the electron capture region of the ejecta; the relatively narrow width ($\sim3{,}000 \, \mathrm{km \, s^{-1}}$) of this line provides further support of this finding. Thus, the existence of the [NiII] line implies ignition at high density, which would supports the Chandra model (Nomoto et al. 2013).

5.2   **Chemical Evolution of Galaxies and Supernova Remnants**

SNe Ia are important to cosmic chemical evolution due to their delayed production of iron-peak elements. Then, the evolution of certain elements can reflect the role of SNe Ia in chemical enrichment. Manganese is one of the important elements to constrain the SNe Ia model. Figure 20 shows the evolution of Manganese as a function of metallicity (Leung and Nomoto 2017b) where the galactic chemical evolution is calculated as described in Leung and Nomoto (2017a).

The stellar abundances are taken from galactic disk F and G dwarfs (Reddy et al. 2003), cluster and field stars (Sobeck et al. 2006) and from thin discs (Feltzing et al. 2007). At low metallicity, [Mn/Fe] does not vary much because of the delay effects. Notice that a white dwarf cannot give rise to SNe Ia instantaneously after the formation of the progenitor WD. The CO WD have masses have masses from 0.6 to 1.0 $M_\odot$. The mass accretion from its companion star in the single-degenerate scenario starts after the companion star ($\leq 8M_\odot$) has evolved slightly off the main-sequence star and become a red giant. per year). Hence, after the formation of WD in the primary star, another 10^{6-10} years are required for the WD to gain mass till the Chandrasekhar mass. Therefore, there is a delay in the first SNe Ia event since the progenitor star is formed. When $Z > 0.1 Z_\odot$ the [Mn/Fe] ratio increases quickly, demonstrating that the SNe Ia is an vital source for manganese to explain the evolution of manganese abundance.
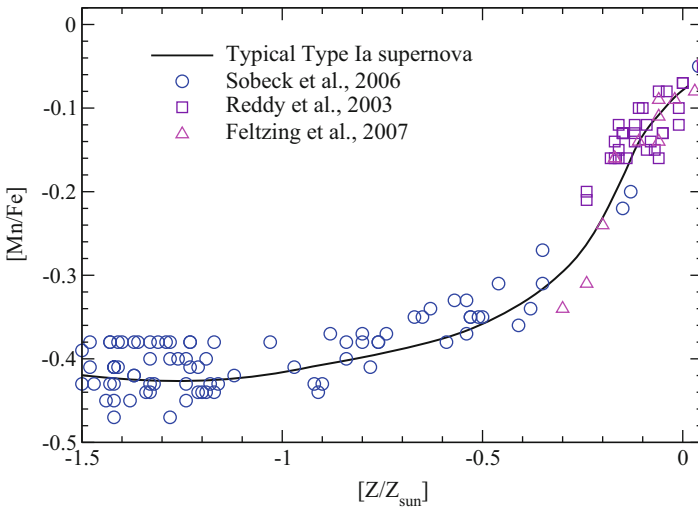

Fig. 20 [Mn/Fe] against [Fe/H] in Galactic chemical evolution (Leung and Nomoto 2017a,b). The numerical models are chosen based on three criteria. 1. The SNe Ia model should be able to represent the normal SNe Ia in general, namely ^{56}Ni about 0.6 $M_\odot$. 2. The manganese should be able to explain the solar abundance in the galactic chemical evolution model. 3. The nickel should satisfy the constraints from the solar abundance
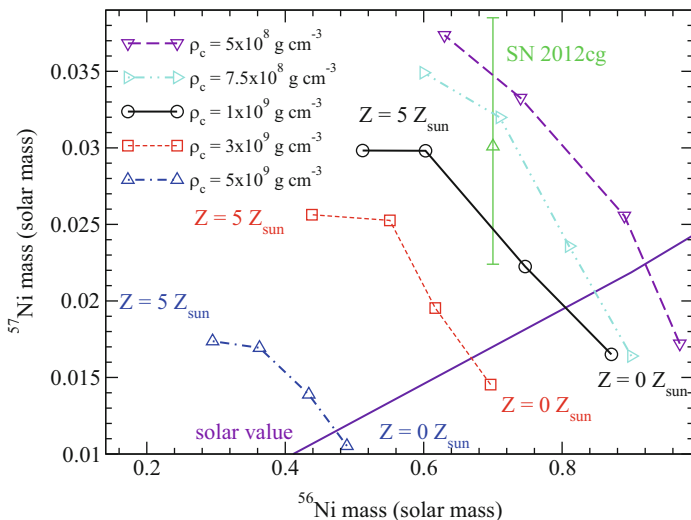
Fig. 21 ^{57}Ni against ^{56}Ni for models with different central densities and metallicity of 0, 1, 3 and 5 $Z_\odot$ (Leung and Nomoto 2017b). The configuration is chosen based on the benchmark model as shown in Fig. 20. The observational data from SN 2012cg (Graur et al. 2016) is shown.

Besides galactic chemical evolution, the model parameter of an individual SN Ia explosion can be studied by looking at the supernova remnant or from its decay lines. Given the observational data, for example isotopes of Ni by the nickel decay, or manganese as from the decayed remnants, constraints on the supernova properties can be derived. In Fig. 21 the mass fractions ^{57}Ni against ^{56}Ni for different central densities is plotted. The observational data from a recent SNe Ia, the SN 2012cg (Graur et al. 2016), is included in the figure. This SNe Ia is regarded as one of the typical SNe Ia with normal luminosity based on its optical signals, i.e. light curves and spectra. By spanning different parameters to look for the model with similar production of ^{57}Ni against ^{56}Ni, this SN Ia has a rather low central density at the moment of explosion. In contrast, it has a high metallicity (five times of the solar metallicity). This demonstrates how one can extract the stellar properties through the use of chemical abundance.

Another example is the observational data from SNe Ia remnant 3C 397. In Figure 22 the [Mn/Fe] ratio against [Ni/Fe] ratio of different SNe Ia models and of the SNe Ia remnant 3C 397 (Yamaguchi et al. 2015) is plotted. Using the nucleosynthesis data from many SNe Ia models, one can predict the SNe Ia progenitor. In particular, the supernova remnant shows strong hints on its high central density and high metallicity, at the moment of its explosion. Certainly, the above two models demonstrate only the preliminary in searching for stellar parameters. Degeneracy may still persist by other configurations such as different initial flame. The degeneracy can be resolved when more than one isotopes or elements are involved in the comparison.
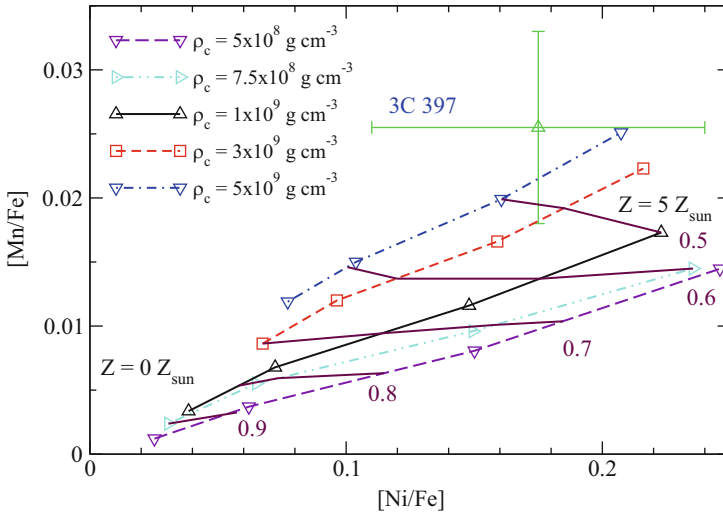
Fig. 22 [Ni/Fe] against [Mn/Fe] for models with different central densities and metallicity of 0, 1, 3 and 5 $Z_\odot$ (Leung and Nomoto 2017b). Similar to Fig. 21, the models are chosen based on the benchmark model in Fig. 20. The observational data from 3C 397 (Yamaguchi et al. 2015) is shown. The purple lines stand for the contours of constant M_{Ni} models.

6   Cross-References

▶ Electron Capture Supernovae from Super Asymptotic Giant Branch Stars
▶ Evolution of Accreting White Dwarfs to the Thermonuclear Runaway
▶ Nucleosynthesis in Thermonuclear Supernovae
▶ Type Ia Supernovae
▶ Type Iax Supernovae

Appendix: A Short Review of Detonation Physics

Deflagration to Detonation Transition

In the previous section why the deflagration phase is necessary and how to implement the flame physics in SNe Ia simulation are discussed. In this section the motivation of including detonation in the framework, its background physics, and the implementation technique are further discussed.

The multidimentional turbulent flame model attempts to introduce a flame-acceleration scheme which allows the flame to burn more material before the expansion of the WD quenches the flame. It is found that the multidimentional PTD model predicts a significant amount of unburnt carbon and oxygen in the central region. As a result, the explosion energy inclines to the weaker side of the observed explosion.

If the transition of deflagration to detonation occurs, the above problem might be solved. Detonation wave is the propagation of burning through shock compression. Unlike the deflagration counterpart, the supersonic motion of detonation can ensure that all necessary material in WD is burnt before the density becomes too low to sustain nuclear burning. This also bypasses the inconsistency of pure detonation model which tends to overproduce ^{58}Ni and ^{54}Fe due to electron capture (see Figs. 9 vs. 10, and Figs. 16 vs. 14) because in DDT model, deflagration part is confined in small mass region and the detonation mostly burns the outer material, which has too low density for electron capture to take place.

Physics of Detonation and Transition

The detonation in general consists of three parts, the pre-shock region, the reaction zone, and the post-reaction zone region. To study the detonation structure, one usually solve the eigenstate(s) for the steady-state detonation wave structure equations (Sharpe 1999).

By assuming the matter remains in thermodynamics equilibrium, that

$$\Delta\varepsilon = \frac{\partial\varepsilon}{\partial\rho}|_{T,X_i} + \frac{\partial\varepsilon}{\partial T}|_{\rho,Y_i} + \sum_i \frac{\partial\varepsilon}{\partial Y_i}|_{\rho,T}, \tag{4}$$

the steady-state Euler equation can be written as

$$\frac{d\rho}{dx} = -\frac{\rho a_f^2}{v}\frac{\boldsymbol{\sigma}\cdot\mathbf{R}}{\iota}, \tag{5}$$

$$\frac{dT}{dx} = \left(\frac{\partial p}{\partial T}\right)_{\rho,Y}^{-1}\left\{\left[u^2 - \left(\frac{\partial p}{\partial\rho}\right)_{T,Y}\right]\frac{d\rho}{dx} - \sum_{i=1}^{N}\left(\frac{\partial p}{\partial X_i}\right)_{\rho,T,Y_{j\neq i}}\frac{dY_i}{dx}\right\}, \tag{6}$$

$$\frac{dY}{dx} = \frac{R}{v}, \tag{7}$$

where

$$\eta = a_f^2 - v^2 \tag{8}$$

is the sonic parameter,

$$a_f^2 = \left(\frac{\partial p}{\partial\rho}\right)_{T,Y} + \left[\frac{p}{\rho^2} - \left(\frac{\partial\varepsilon}{\partial\rho}\right)_{T,Y}\right]\left(\frac{\partial p}{\partial T}\right)_{\rho,T}\left(\frac{\partial\varepsilon}{\partial T}\right)_{\rho,Y}^{-1} \tag{9}$$

is the sound speed of constant composition (also known as frozen sound speed in the literature of detonation), and

$$\sigma_i = \frac{1}{\rho a_f^2} \left\{ \left(\frac{\partial p}{\partial Y_i}\right)_{\rho,T,Y_{j\neq i}} - \left(\frac{\partial p}{\partial T}\right)_{\rho,Y} \left(\frac{\partial \varepsilon}{\partial T}\right)_{\rho,Y}^{-1} \right.$$

$$\left. \left[\left(\frac{\partial \varepsilon}{\partial Y_i}\right)_{\rho,T,Y_{j\neq i}} - \left(\frac{\partial q}{\partial Y_i}\right)_{Y_{j\neq i}} \right] \right\} \tag{10}$$

is the thermicity constant, such that $\sigma \cdot \mathbf{R}$ is the thermicity.

It should be noted that at Eq. (7), the denominator η can bring subtlety to the calculation. In Chapman-Jouget detonation, η is always positive that the solution is continuous everywhere. However, for realistic equation of states and network, η can change sign. It corresponds to the point that the fluid velocity equals to the frozen speed of sound. At this point, there are two solutions for the detonation. First, by direct integration, the zone beyond that points has supersonic velocity. This corresponds to self-sustained detonation wave. Second, the reaction zone remains to be subsonic everywhere. This produces cusps in both density and temperature at that point, so that the solution remains continuous while satisfying the above equations.

In general, only the second solution represents the stable detonation wave which occurs in SNe Ia. In Fig. 23 the density and temperature of a typical detonation wave is plotted. After the shock, there is a buffer zone which allows the temperature to increase. Once the matter reaches 4×10^9 K, the burning of carbon and oxygen becomes explosive that the temperature can be doubled within a few 10^{-2} cm. At about 0.1 cm, the drop of density has significantly led to a jump in the fluid
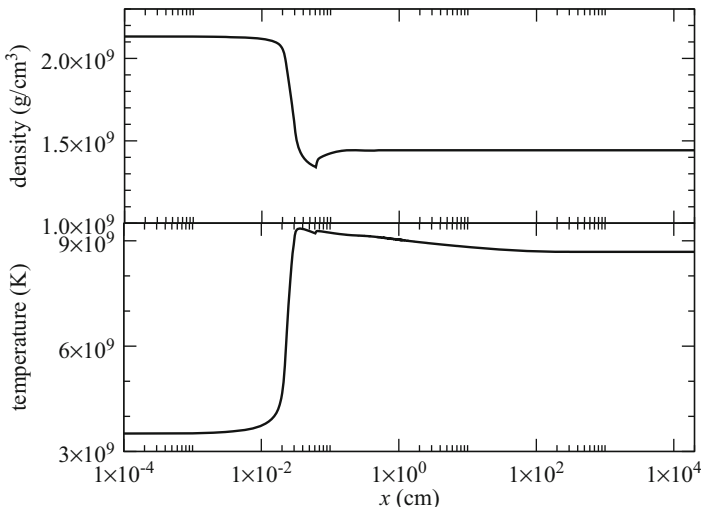

Fig. 23 *Upper panel*: The density profile of the detonation wave at density 10^9 g cm^{-3}. The detonation is assumed to start with a post-shock temperature 3.5×10^9 K with a composition 50 %^{12}C and 50 %^{16}O by mass. *Lower panel*: Same as above, but for the temperature profile
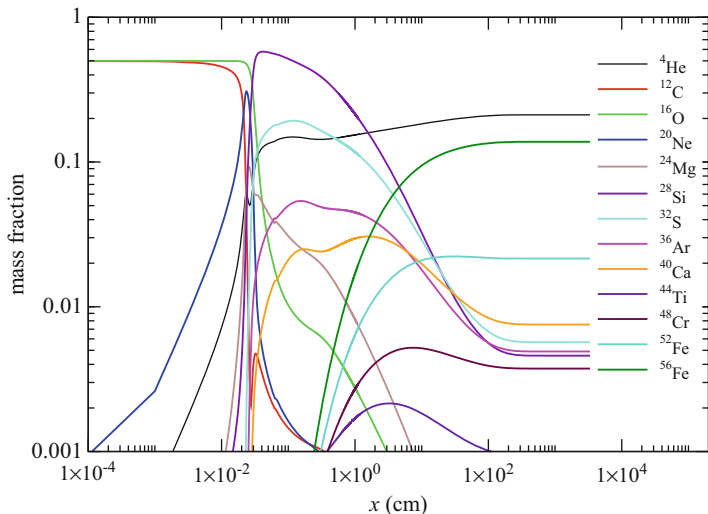
Fig. 24 The chemical profile of the detonation wave for a detonation wave at density 10^9 g cm^{-3}

velocity, due to mass conservation. This makes the wave reach the frozen sound speed. At that point, the solution to the pathological detonation is connected, which ensures the ash propagates subsonic everywhere. The density reaches its equilibrium ~ 1 cm, while the temperature reaches equilibrium at about 10^2 cm. In Fig. 24 the abundance profile for the same detonation wave is plotted. Similar to deflagration, at $x < 10^{-2}$ cm, ^{12}C burns to form ^{20}Ne and ^{4}He. At $10^{-2} < x < 10^{-1}$ cm, both carbon and oxygen burning produce intermediate mass isotopes such as ^{32}S, ^{36}Ar, ^{40}Ca, and ^{44}Ti. At $10^{-2} < x < 10^2$ cm, the matter slowly converts to NSE that iron-peak isotopes, including ^{48}Cr, ^{52}Fe, and ^{56}Ni form. The matter reaches equilibrium and no net change is observed beyond $x > 10^2$ cm.

In SNe Ia simulations, the detonation energy and composition table need to be computed prior to the hydrodynamics simulations. This is because the table includes solving the equations for the detonation wave structure in order to find the energy release, propagation velocity for the pathological detonation, and ash composition as a function of density. In general, it depends on temperature as well. Owing to the electron degeneracy and that the nuclear binding energy change is much larger than the matter internal energy, the exact yield is less sensitive to the choice of temperature than that of density. After that, similar to the deflagration, the front is tracked by some discontinuity tracking scheme. By extracting the geometric properties of the front, corresponding energy and composition of the fluid swept by detonation wave are changed.

One technical difference between deflagration and detonation is that detonation does not start at the beginning of the simulation and requires certain trigger. In practice, detonation is assumed to start when the local Karlovitz number Ka ≥ 1, namely, the ratio between turbulence length scale and the flame width. When it is
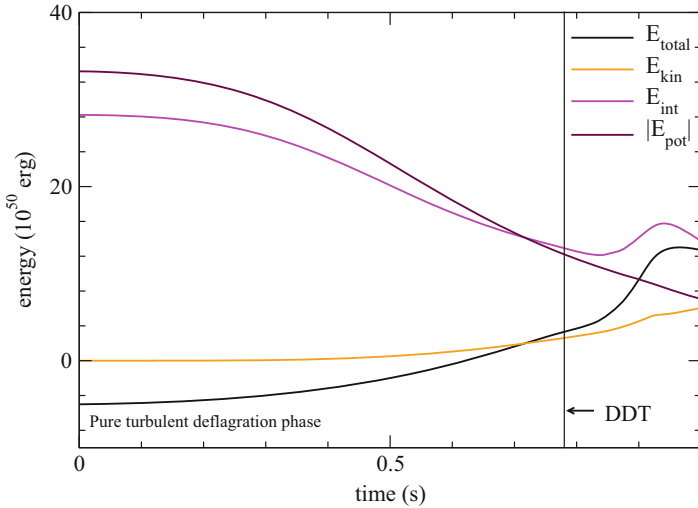
Fig. 25 The time evolution of the total, kinetic, internal, and potential energy of the same model as in Fig. 13

satisfied, the eddies around the thick flame becomes important to diffuse the heat from the hot ash to the cold fuel and cease the explosive burning. The hot region can carry out carbon burning simultaneously, creating a supersonic pulse and the shock. The shock then develops into detonation and burns the remaining fuel.

To demonstrate the technique in carrying out detonation physics in Type Ia supernova simulations, a two-dimensional hydrodynamics simulation for the explosion phase of a carbon-oxygen core is presented. The configuration is similar to the model in Sect. 4.1. In Fig. 25 the energy evolution is plotted. The phase before DDT that has started is exactly the same as the PTD model since the same initial model and flame physics are used. But once DDT is triggered, the two models deviate. The total energy increases much faster to a much higher equilibrium value. It also leads to the global heating of matter, as shown by the increase of internal energy. Kinetic energy also continues to grow, in contrast to the asymptotic behavior as shown in the PTD counterpart.

Open Questions in Detonation

It should be noted that there are two outstanding questions in the detonation transition remain unresolved. In one way, detonation transition is shown to be possible in the form of shock compression in a closed system and by turbulent compression in an open system. Certainly, the environment of a WD belongs to the latter one, where turbulent diffusion is relied to generate a smeared hot spot which can undergo supersonic heating. However, in the large-eddy simulations, it

is shown that the typical turbulence strength is only marginally strong to diffuse the thermal energy. In terms of power spectrum, the probability of finding a fluid element with the required velocity fluctuation is small. Certainly, in most SNe Ia simulation, subgrid turbulence are used to estimate the turbulent kinetic energy. This points to the uncertainty in the subgrid turbulence model. Future work in how to achieve a robust turbulence model will offer important insight to the feasibility of the DDT model. Second, the exact Karlovitz number for DDT is not exactly known. In SNe Ia simulation in the literature, typical value of Ka $\approx$ 1. However, in direct numerical simulation of DDT for the H_2-air flame, at least Ka $=$ 100 is required. Certainly, a one-one correspondence between the H_2-air flame and the carbon-oxygen flame cannot be drawn straightforwardly due to the huge differences in the equation of states and reaction channel. Despite that, the terrestrial flame experiment has demonstrated that the detonation transition can be much harder than one has assumed. It is therefore necessary to understand the critical Ka for DDT transition for a carbon-oxygen WD and if it can be achieved in hydrodynamics simulation.

References

Arnett D (1969) A possible model of supernovae: detonation of 12C. Ap & SS 5:180–212

Arnett D (1996) Supernovae and nucleosynthesis. Princeton University Press, Princeton

Benvenuto OG, Panei JA, Nomoto K, Kitamura H, Hachisu I (2015) Final evolution and delayed explosions of spinning white dwarfs in single degenerate models for Type Ia supernovae. ApJL 809:L6

Denissenkov PA, Herwig F, Truwan JW et al (2013) The C-flame quenching by convective boundary mixing in super-AGB stars and the formation of hybrid C/O/Ne white dwarfs and SN progenitors. ApJ 772:37–45

Dilday B, Howell DA, Cenko SB et al (2012) PTF 11kx: A Type Ia supernova with a symbiotic nova progenitor. Science 337:942

Di Stefano R, Voss R, Claeys JSW (2011) Spin-up/spin-down models for Type Ia supernovae. ApJL 738:L1

Fink M, Kromer M, Seitenzahl IR et al (2014) Three-dimensional pure deflagration models with nucleosynthesis and synthetic observables for Type Ia supernovae. MNRAS 438:1762–1782

Foley RJ, Simon JD, Burns CR et al (2012) Linking Type Ia supernova progenitors and their resulting explosions. ApJ 752:101

Hachisu I, Kato M (2001) Recurrent novae as a progenitor system of Type Ia supernovae. I. RS Ophiuchi subclass: systems with a red giant companion. ApJ 558:323

Hachisu I, Kato M, Nomoto K (1996) A new model for progenitor systems of Type Ia supernovae. ApJL 470:97

Hachisu I, Kato M, Nomoto K, Umeda H (1999a) A new evolutionary path to Type IA supernovae: a helium-rich supersoft X-ray source channel. ApJ 519:314

Hachisu I, Kato M, Nomoto K (1999b) A wide symbiotic channel to Type IA supernovae. ApJ 522:487

Hachisu I, Kato M, Nomoto K (2008a) Young and massive binary progenitors of Type Ia supernovae and their circumstellar matter. ApJ 679:1390–1404

Hachisu I, Kato M, Nomoto K (2008b) The delay-time distribution of Type Ia supernovae and the single-degenerate model. ApJ 683:L27

Hachisu I, Kato M, Nomoto K (2012a) Final fates of rotating white dwarfs and their companions in the single degenerate model of Type Ia supernovae. ApJL 756:L4

Hachisu I, Kato M, Saio H, Nomoto K (2012b) A single degenerate progenitor model for Type Ia supernovae highly exceeding the Chandrasekhar mass limit. ApJ 744:69

Hamuy M, Phillips MM, Suntzeff NB et al (2003) An asymptotic-giant-branch star in the progenitor system of a Type Ia supernova. Nature 424:651

Han Z, Podsiadlowski Ph (2004) The single-degenerate channel for the progenitors of Type Ia supernovae. MNRAS 350:1301

Hillebrandt W, Niemeyer JC (2000) Type Ia supernova explosion models. ARAA 38:191

Iben I Jr, Tutukov AV (1984) Supernovae of Type I as end products of the evolution of binaries with components of moderate initial mass (M not greater than about 9 solar masses). ApJS 54:335

Ilkov M, Soker N (2012) Type Ia supernovae from very long delayed explosion of core-white dwarf merger. MNRAS 419:1695

Iwamoto K, Brachwitz F, Nomoto K et al (1999) Nucleosynthesis in Chandrasekhar mass models for Type IA supernovae and constraints on progenitor systems and burning-front propagation. ApJS 125:439–463

Justham S (2011) Single-degenerate Type Ia supernovae without hydrogen contamination. ApJL 730:L34

Kamiya Y, Tanaka M, Nomoto K et al (2012) Super-Chandrasekhar-mass light curve models for the highly luminous Type Ia supernova 2009dc. ApJ 756:191

Kato M, Saio H, Hachisu I, Nomoto K (2014) Shortest recurrence periods of novae. ApJ 793:136

Khokhlov AM (1991) Delayed detonation model for Type IA supernovae. A & A 245: 114–128

Kitamura H (2000) Pycnonuclear reactions in dense matter near solidification. ApJ 539:888

Kitaura FS, Janka H-Th, Hillebrandt W (2006) Explosions of O-Ne-Mg cores, the Crab supernova, and subluminous type II-P supernovae. A & A 450:345

Krause O, Tanaka M, Usuda T, Hattori T, Goto M, Birkmann S, Nomoto K (1997) Tycho Brahe's 1572 supernova as a standard Type Ia as revealed by its light-echo spetraum. Nature 456:617

Kromer M, Fink M, Stanishev V (2013) 3D deflagration simulations leaving bound remnants: a model for 2002cx-like Type Ia supernovae. MNRAS 429:2287–2297

Kromer M, Ohlmann ST, Pakmor R et al (2015) Deflagrations in hybrid CONe white dwarfs: a route to explain the faint Type Iax supernova 2008ha. MNRAS 450:3045–3053

Langer N, Deutschmann A, Wellstein S, Höflich P (2000) The evolution of main sequence star + white dwarf binary systems towards Type Ia supernovae. A & A 362:1046

Leung S-C, Nomoto K (2017a) Nucleosynthesis of iron-peak elements in Type-Ia supernovae. JPS Conf Proc 14:020506

Leung S-C, Nomoto K (2017b) Dependence of nucleosynthesis on model parameters of Type Ia supernovae. ApJ (submitted)

Leung S-C, Chu M-C, Lin L-M (2015a) A new hydrodynamics code for Type Ia supernovae. MNRAS 454:1238

Leung S-C, Chu M-C, Lin L-M (2015b) Dark matter admixed Type Ia supernovae. MNRAS 812:110

Li X-D, van den Heuvel EPJ (1997) Evolution of white dwarf binaries: supersoft X-ray sources and progenitors of Type IA supernovae. A & A 322:L9

Li W, Bloom JS, Podsiadlowski P et al (2011) Exclusion of a luminous red giant as a companion star to the progenitor of supernova SN 2011fe. Nature 480:348

Livio M (2000) The progenitors of Type Ia supernovae. In: Niemeyer JC, Truran JW (eds) Type Ia supernovae, theory and cosmology. Cambridge University Press, Cambridge, p 33

Maeda K et al (2010) An asymmetric explosion as the origin of spectral evolution diversity in Type Ia supernovae. Nature 466:82

Maoz D, Mannucci F, Nelemans G (2014) Observational clues to the progenitors of Type Ia supernovae. ARAA 52:107

Mori K et al (2016) Impact of new Gamow-Teller strengths on explosive Type Ia supernova nucleosynthesis. ApJ 833:179

Nomoto K (1982) Accreting white dwarf models for Type I supernovae. I – presupernova evolution and triggering mechanisms. ApJ 253:798

Nomoto K, Sugimoto D, Neo S (1976) Carbon deflagration supernova, an alternative to carbon detonation. Ap & SS 39:L37–L42

Nomoto K, Nariai K, Sugimoto D (1979) Rapid mass accretion onto white dwarfs and formation of an extended envelope. PASJ 31:287

Nomoto K, Thielemann F-K, Yokoi K (1984) Accreting white dwarf models of Type I supernovae. III – carbon deflagration supernovae. ApJ 286:644–658

Nomoto K, Yamaoka H, Shigeyama T, Kumagai S, Tsujimoto T (1994) Type I supernovae and evolution of interacting binaries. In: Bludmann S et al. (eds) Proceedings of session LIV held in Les Houche 1990. Supernovae, NATO ASI series C, vol 199. North-Holland

Nomoto K, Iwamoto K, Kishimoto N (1997) Type Ia supernovae: their origin and possible applications in cosmology. Science 276:1378

Nomoto K, Umeda H, Kobayashi C et al (2000a) Type Ia supernova progenitors, environmental effects, and cosmic supernova rates. In: Niemeyer JC and Truran JW (eds) Type Ia Supernovae, Theory and Cosmology, Cambridge University Press, p.63

Nomoto K, Umeda H, Kobayashi C et al (2000b) Type Ia supernovae: progenitors and evolution with redshift. In: Cosmic Explosions: AIP Conf Proc 522:35

Nomoto K, Suzuki T, Deng J, Uenishi T, Hachisu I (2005) Progenitors of Type Ia Supernovae: circumstellar interaction, rotation, and steady hydrogen burning. In: Turatto et al (eds) 1604-2004: Supernovae as Cosmological Lighthouses, ASP conference series, 342:105

Nomoto K, Saio H, Kato M, Hachisu I (2007) Thermal stability of white dwarfs accreting hydrogen-rich matter and progenitors of Type Ia supernovae. ApJ 663:1269

Nomoto K, Kamiya Y, Nakasato N et al (2009) Progenitors of Type Ia supernovae: single degenerate and double degenerates. AIPC 1111:267

Nomoto K, Kamiya M, Nakasato N (2013) Type Ia supernova models and progenitor scenarios. In: Di. Stefano R et al (eds) IAU Symposium 281, Binary Paths to Type Ia Supernovae Explosions, Cambridge University Press, Cambridge, p. 253–260

Nugent P et al (2000) Synthetic spectra of hydrodynamical models of Type Ia supernovae. ApJ 485:812

Patat F, Chandra P, Chevalier R et al (2007) Detection of circumstellar material in a normal Type Ia supernova. Science 317:924

Plewa T (2007) Detonating failed deflagration model of thermonuclear supernovae. I. Explosion dynamics. ApJ 657:942–960

Pocheau A (1994) Scale invariance in turbulent front propagation. PRE 49:1109–1122

Potekhin AY, Chabrier G (2012) Thermonuclear fusion in dense stars. Electron screening, conductive cooling, and magnetic field effects. Astron Astropart 538:AA115

Schaefer BE, Pagnotta A (2012) An absence of ex-companion stars in the Type Ia supernova remnant SNR 0509-67.5. Nature 481:164

Schmidt W, Niemeyer JC, Hillebrandt W, Roepke FK (2006) A localised subgrid scale model for fluid dynamical simulations in astrophysics. II. Application to Type Ia supernovae. A & A 450:283–294

Schwab J, Quataert E, Bildsten L (2015) Thermal runaway during the evolution of ONeMg cores towards accretion-induced collapse. MNRAS 453:1910–1927

Seitenzahl IR, Kromer M, Ohlmann ST et al (2016) Three-dimensional simulations of gravitationally confined detonations compared to observations of SN 1991T. A & A 592:A57

Sharpe GJ (1999) The structure of steady detonation waves in Type Ia supernovae: pathological detonations in C+O cores. MNRAS 310:1039–1052

Shen K, Bildsten L (2007) Thermally stable nuclear burning on accreting white dwarfs. ApJ 660:1444

Shigeyama T, Nomoto K, Yamoka H, Thielemann F-K (1992) Possible models for the Type IA supernova 1990N. ApJL 386:13

Sternberg A, Gal-Yam A, Simon JD et al (2011) Circumstellar material in Type Ia supernovae via sodium absorption features. Science 333:856

Webbink RF (1984) Double white dwarfs as progenitors of R Coronae Borealis stars and Type I supernovae. ApJ 277:355

Yamaguchi H et al (2015) A Chandrasekhar mass progenitor for the Type Ia supernova remnant 3C 397 from the enhanced abundances of Nickel and Manganese. ApJ 801:L31

Further Reading

Barth TJ, Deconinck H (1999) High-order methods for computational physics. Lecture notes in computational science and engineering, vol 9. Springer, New York

Calder AC, Townsley DM, Seitenzahl IR et al (2007) Capturing the fire: flame energetics and neutronization for Type Ia supernova simulations. ApJ 656:313–332

Clement MJ (1993) Hydrodynamical simulations of rotating stars. I – A model for subgrid-scale flow. ApJ 406:651–660

Feltzing S, Fohlman M, Bensby T (2007) Manganese trends in a sample of thin and thick disk stars. The origin of Mn. A & A 467:665

Förster F, Lesaffre P, Podsiadlowski P (2010) Simplified hydrostatic carbon burning in white dwarf interiors. ApJS 190:334

Garcia-Senz D, Woosley SE (1995) Type IA supernovae: the flame is born. ApJ 454:895–900

Golombek I, Niemeyer JC (2005) A model for multidimensional delayed detonations in SN Ia explosions. A & A 438:611–616

Graur O et al (2016) Late-time photometry of Type Ia supernova SN 2012cg reveals the radioactive decay of 57 Co. ApJ 819:31

Hachisu I (1986) A versatile method for obtaining structures of rapidly rotating stars. ApJS 61:479

Hicks EP (2015) Rayleigh-Taylor unstable flames – fast or faster? ApJ 803:72

Jackson AP, Townsley DM, Calder AC (2014) Power-law wrinkling turbulence-flame interaction model for astrophysical flames. ApJ 784:174

Kerzendorf WE, Schmidt BP, Asplund M et al (2009) Subaru high-resolution spectroscopy of star G in the Tycho supernova remnant. ApJ 701:1665

Kerzendorf WE, Schmidt BP, Laird JB et al (2012) Hunting for the progenitor of SN 1006: high-resolution spectroscopic search with the FLAMES instrument. ApJ 759:7

Khokhlov AM, Oran E, Wheeler JC (1997) Deflagration-to-detonation transition in thermonuclear supernovae. ApJ 478:678–688

Kobayashi C, Nakasato N (2011) Chemodynamical simulations of the milky way galaxy. ApJ 729:16

Lesaffre P, Podsiadlowski P, Tout CA (2005) A two-stream formalism for the convective Urca process. MNRAS 356:131

Likewski AM, Hillebrandt W, Woosley SE et al (2000) Distributed burning in Type Ia supernovae: a statistical approach. ApJ 503:405–413

Livne E, Asida SM, Hoeflich P (2005) On the sensitivity of deflagrations in a Chandrasekhar mass white dwarf to initial conditions. ApJ 632:443–449

Maeda K et al (2010) Nebular spectra and explosion asymmetry of Type Ia supernovae. ApJ 708:1703

Maeder A (2009) Physics, formation and evolution of rotating stars. Springer, Berlin

Mazzali PA, Sullivan M, Filippenko AV et al (2015) Nebular spectra and abundance tomography of the Type Ia supernova SN 2011fe: a normal SN Ia with a stable Fe core. MNRAS 450:2631

Niemeyer JC, Hillebrandt W (1995) Turbulent nuclear flames in Type IA supernovae. ApJ 452:769–778

Nomoto K (1982) Accreting white dwarf models for Type 1 supernovae. II – off-center detonation supernovae. ApJ 257:780

Nomoto K, Kondo Y (1991) Conditions for accretion-induced collapse of white dwarfs. ApJL 367:19–22

Nomoto K, Suzuki T, Deng J, Uenishi T, Hachisu I, Mazzali P (2004) Circumstellar interaction of Type Ia supernova SN 2002ic. Front Astropart Phys Cosmol: RESCEU Int Symp Ser 6:323

Ostriker JP, Bodenheimer P (1968) Rapidly rotating stars. II. Massive white dwarfs. ApJ 151:1989

Pakmor R, Kromer M, Roepke FK et al (2010) Sub-luminous Type Ia supernovae from the mergers of equal-mass white dwarfs with mass 0.9 Msolar. Nature 463:61

Piersanti L, Gagliardi S, Iben I, Tornambe A (2003) Carbon-oxygen white dwarf accreting cO-rich matter. II. Self-regulating accretion process up to the explosive stage. ApJ 598:1229

Piro AL (2008) The internal shear of Type Ia supernova progenitors during accretion and simmering. ApJ 679:616

Poludenko AY, Gardiner TA, Oran ES (2011) Spontaneous transition of turbulent flames to detonations in unconfined media. PRL 107:054501

Reddy BE, Tomkin J, Lambert DL, Allende Prieto C (2003) The chemical compositions of galactic disc F and G dwarfs. MNRAS 340:304

Reinecke M, Hillebrandt W, Niemeyer JC et al (1999a) A new model for deflagration fronts in reactive fluids. A & A 347:724–733

Reinecke M, Hillebrandt W, Niemeyer JC (1999b) Thermonuclear explosions of Chandrasekhar-mass C+O white dwarfs. A & A 347:739–747

Reinecke M, Hillebrandt W, Niemeyer JC (2002) Three-dimensional simulations of Type Ia supernovae. A & A 391:1167–1172

Roepke FK (2007) Flame-driven deflagration-to-detonation transitions in Type Ia supernovae? ApJ 668:1103–1108

Rueda JA, Boshkayev K, Izzo L et al (2013) A white dwarf merger as progenitor of the anomalous X-ray pulsar 4U 0142+61?. ApJL 772:L24

Saio H, Nomoto K (2004) Off-center carbon ignition in rapidly rotating, accreting carbon-oxygen white dwarfs. ApJ 615:444

Seitenzahl IR et al (2013) Solar abundance of manganese: a case for near Chandrasekhar-mass Type Ia supernova progenitors. A & A 559:L5

Sethian JA (1996) Level set method. Cambridge University Press, Cambridge

Shih T-H, Liou WW, Shabbir A et al (1994) A new $k - \varepsilon$ eddy viscosity model for high reynolds number turbulent flows. Comput Fluids 24:227–238

Shih T-H, Zhu J, Lumley JL (1995) A new Reynolds stress algebraic equation model. Comput Methods Appl Mech Eng 125:287–302

Sobeck JS, Ivans II, Simmerer JA et al (2006) Manganese abundances in cluster and field stars. AJ 131:2949

Timmes FX (2000) Physical properties of Laminar Helium deflagrations. ApJ 528:913–945

Timmes FX, Woosley SE (1992) The conductive propagation of nuclear flames. I – degenerate C + O and O + NE + MG white dwarfs. ApJ 396:649–667

Townsley DM, Calder AC, Asida SM et al (2007) Flame evolution during Type Ia supernovae and the deflagration phase in the gravitationally confined detonation scenario. ApJ 668:1118–1131

Uenishi T, Nomoto K, Hachisu I (2003) Evolution of rotating accreting white dwarfs and the diversity of Type Ia supernovae. ApJ 595:1094

Wang R, Spiteri RJ (2007) Linear instability of the fifth-order WENO method. SIAM J Numer Anal 45:1871

Wang B, Justham S, Liu Z-W et al (2014) On the evolution of rotating accreting white dwarfs and Type Ia supernovae. MNRAS 445:2340

Woosley SE, Weaver TA (1994) Sub-Chandrasekhar mass models for Type IA supernovae. ApJ 423:371

Wunsch W, Woosley SE (2004) Convection and off-center ignition in Type Ia supernovae. ApJ 616:1102–1108

Yoon S-C, Langer N (2004) Presupernova evolution of accreting white dwarfs with rotation. A & A 419:623

Yoon S-C, Langer N (2005) On the evolution of rapidly rotating massive white dwarfs towards supernovae or collapses. A & A 435:967

Zhang Y (2009) A two-dimensional flame tracking algorithm with application to Type Ia supernova. Nonlinear Phys 22:1909–1925

Zingale M, Dursi LJ (2007) Propagation of the first flames in Type Ia supernovae. ApJ 656:333–346

Zingale M, Nonaka A, Almgren AS et al (2011) The convective phase preceding Type Ia supernovae. ApJ 740:8–25